

Chapter 1

Study of inelastic processes in ion-H₂O collisions using classical (CTMC) and semiclassical methods

L.F. Errea, Clara Illescas, P. M. M. Gabás, L. Méndez, I. Rabadán, A. Riera,

Laboratorio Asociado al CIEMAT de Física Atómica y Molecular en Plasmas de Fusión.

Departamento de Química, módulo 13, Universidad Autónoma de Madrid, Cantoblanco 28049-Madrid, Spain

lf.errea@uam.es

B. Pons

CELIA, Université de Bordeaux I-CNRS-CEA, 351 Cours de la Libération, 33405-Talence, France

We present calculations of cross sections for one- and two-electron processes in collisions of H⁺, He²⁺ and C⁶⁺ with water molecules. We employ two kind of methods: a classical trajectory Monte Carlo (CTMC) approach and a semiclassical treatment with expansions in terms of molecular wavefunctions. Anisotropy effects related to the structure of the target are explicitly incorporated by using a three-center model potential to describe the electron-H₂O⁺ interaction. This is compared with a simple approach that employs a screened Coulomb potential. At high energies we derive scaling laws with respect to the projectile charge. We also estimate cross sections for molecular fragmentation subsequent to electron removal.

1. Introduction

Hadron therapy is a valuable alternative to X- or γ -ray radiotherapy (see Refs. [1, 2] for reviews). The use of this technique started in 1954 at the Lawrence Berkeley Laboratory (USA) [3]; since then, several thousands of patients have been treated with proton beams in several installations and with carbon ion ones at Chiba (Japan) [4] and Darmstadt (Germany) [5]. These techniques have several advantages when compared to conventional

photon radiation: they allow access to deeply seated tumors, and the lethal tumor dose is raised while the surrounding healthy tissue remains unaffected. Physicists and biologists can measure and/or compute the intensity, penetration depth and lethal dose of the ion beams [6–9]. The mechanisms responsible for single and double strand breaks of the DNA, which subsequently lead to cell death, are complex, and several works (see Ref. [10] and references therein) have aimed to elucidate them. The interest of this subject has motivated experiments on collisions of multicharged ions with DNA bases to shed light on the DNA fragmentation processes (see, e.g., Ref. [11]), but theoretical works are scarce [12, 13].

On the other hand, e-DNA experiments [14] have shown that collisions of relatively slow electrons (with energy of about 10 eV) can lead to the breakdown of DNA through a mechanism that involves the formation of intermediate resonant states. Therefore, processes that produce electrons are also relevant in the understanding of biological damage and ion therapy. In this respect, electron emission in collisions of ions with water provides the most significant source of electrons in the interaction of ion beams with the cell. Although several experiments have provided detailed information on ionizing proton-water collisions, data are scarce for multicharged ion impact. Furthermore, in addition to target ionization, other processes such as excitation and charge-exchange in ion-H₂O collisions can lead to molecular fragmentation, and the fragments formed in these reactions are also responsible for DNA breakdown. Therefore, these processes must also be explicitly considered to reliably simulate the passage of charged particles in biological environments [15, 16].

Experiments on ion-water collisions include early measurements of total cross sections for electron capture and electron loss of Dagnac *et al.* [17]. Rudd *et al.* measured total cross sections for production of electrons and positive charges in collisions of protons [18–20] and alpha particles [21] with water vapour, at collision energies from a few keV/amu to several MeV/amu. Measurements of total electron capture cross sections at collision energies of about 1 keV/amu have been reported in Refs. [22–24]; these results are particularly relevant in cometary X-ray emission. Recently, the experiments have focused on the molecular fragmentation [25–31], and some works [32, 33] have measured both target and projectile Balmer emission after ion-H₂O collisions.

Previous theoretical works aimed at filling in the collisional database of interest for radiation damage. Nevertheless, most of these works focused on H⁺+H₂O collisions and employed perturbative methods [34], such as the

continuum distorted wave-eikonal initial state (CDW-EIS) [35–37] and first Born (FB) approximations [38], which are in general useful at impact energies E greater than 100 keV/amu. Recently, Lüdde *et al.* [39] have applied the basis set generator method (BGM) to $H^+ + H_2O$ collisions, beyond the isotropic electron-core approximation; they have reported electron production and net capture cross sections in good agreement with experiment.

With respect to collisions of Multicharged ions, $He^{2+} + H_2O$ have been studied in Refs. [40] and [41], in the frameworks of FB and classical models, respectively. Comparison with experimental data showed acceptable, but not very satisfactory, agreement. In spite of the interest of $C^{6+} + H_2O$ collisions in ion-based cancer therapy, only CDW-EIS [42] and FB [43] calculations of the total ionization cross section have been reported so far, together with a single experimental point at 6 MeV/amu [42].

In this work, we consider the use of the classical trajectory Monte Carlo (CTMC) method to evaluate cross sections for single ionization, single capture, and two-electron processes (transfer ionization, double capture and double ionization) in H^+ , He^{2+} , $C^{6+} + H_2O$ collisions in the impact energy range $20 \leq E \leq 10000$ keV/amu, which covers the intermediate and high impact energy regimes of interest for therapy applications. This chapter is mainly based on the work published in Refs. [44] and [45]. Since 1966, when it was first applied to ion-atom collisions [46], the CTMC method has been widely employed to treat ion collisions with one-electron targets. In this respect, previous works of our group, which aimed at providing data sets for plasma diagnostics, considered multicharged ions - H collisions (see Refs. [47–51]). With the exception of a few works [52–54] that dealt with the classical treatment of two-electron systems, the application of the CTMC method to many-electron targets is in general carried out by employing the Independent Particle Model (IPM) [55–57], which assumes that each electron moves in an effective field created by the nuclei and the remaining electrons. In practice, this assumption reduces the solution of the many-electron problem to a set of non-interacting one-electron problems for each electron of the system. In general, the effective potentials are screened-Coulomb potentials with effective charges obtained by fitting the energies of the target electrons. More sophisticated model potentials have been employed in Ref. [58].

A first difference between the application of the CTMC method to ion-molecule and ion-atom collisions is the existence of the target internal degrees of freedom; however, CTMC is usually applied at high collision energies ($E > 25$ keV/amu), where one can assume that the target nuclei

remain fixed during the collision. The main difference with respect to ion-atom collisions is therefore the anisotropy of the target. Previous CTMC calculations for ion-molecule collisions are scarce; they include some calculations of electron capture and ionization cross sections in ion-H₂ [59–61], using one-center potentials. Collisions with H₂O have been considered in the CTMC calculations of Otranto *et al.* [62, 63], who have evaluated state-selective electron capture cross sections at relatively low collision energies, motivated by the application of these data to model cometary X-ray emission. As in practically all available calculations, our treatment employs the IPM, which involves the use of electron-core effective potentials. In a first approach [44] we used one-center (isotropic) potentials. Afterwards, we have developed a technique that uses a three-center model potential to describe the interaction of the active electron with the H₂O⁺ core; this allows us to explicitly consider the anisotropy of the molecular target. In this respect, it is noteworthy that relevant anisotropy effects have been detected in calculations of both H⁺- and *e*-H₂O collisions (see, e.g., Refs. [39, 64]). The evaluation of inelastic probabilities for the physical many-electron system, in terms of the mono-electronic ones resulting from the model potential calculations is usually carried out by means of the IPM. In our work we have also considered the application of the so-called independent event model (IEVM) [65–68], which has been found [69, 70] to be more adequate than the usual IPM for multielectronic targets.

As mentioned above, the application of the CTMC method is restricted to collision energies above 25 keV/amu. At lower energies, one must employ a semiclassical formalism, where the electronic motion is treated quantum-mechanically. Some calculations [71, 72] have used this methodology, expanding the collision wavefunction in terms of the electronic wavefunctions of the supermolecule formed by the ion and the target molecule. Although *ab initio* electronic structure calculations can be performed with high accuracy for relatively small systems like H₂O [73] and H₃O⁺ [74], dynamical calculations require simplified methods to avoid the need of regularizing conical intersections where dynamical couplings diverge (see, e.g. Ref. [75] and references therein), as these regions are the loci where non-adiabatic transitions can predominantly take place at low energies. In this work, we describe and apply two relatively simple semiclassical *ab initio* methods to evaluate charge transfer and ionization cross sections, with the idea that they could be applied to study larger biomolecules. As in the CTMC approach, the two techniques are based on the use of a multi-center pseudo-potential, to describe the interaction of the active electron with the target

polyatomic core, and the IPM to define transition probabilities.

The chapter is organized as follows: In section 2, we summarize the basic assumptions of our CTMC approach, emphasizing the description of the initial electron densities associated to the molecular orbitals. The use of semiclassical methods at relatively high collision energies is considered in section 3. We present in section 4 our results for $\text{H}^+ + \text{H}_2\text{O}$ collisions and compare them to both experimental and theoretical data. We also compare in this section the results obtained from applying the methods explained in sections 2 and 3. Sections 5 and 6 contain our results for He^{2+} and C^{6+} ion impacts, respectively; useful scaling relations with respect to the projectile charge and the impact energy are presented in Section 7. Heavy fragments formed in the dissociation that takes place after molecular ionization are important sources of radiation damage, and we have evaluated fragmentation cross sections for $\text{H}^+ + \text{H}_2\text{O}$ collisions; they are displayed in Section 7. Finally, conclusions and perspectives issued from the present work are given in section 8. Atomic units are used throughout unless otherwise indicated.

2. Impact parameter-CTMC approach

Since we consider relatively high collision energies, we apply the Franck-Condon approximation where the nuclei of the H_2O molecule remain at their equilibrium positions during the collision. Furthermore, we employ the impact parameter approximation [76] in which the relative ion-molecule motion is described by straight-line trajectories $\mathbf{R}(t) = \mathbf{b} + \mathbf{v}t$, where \mathbf{R} is the ion position vector with respect to the origin of coordinates, placed on the oxygen nucleus of the target molecule, \mathbf{b} is the impact parameter and \mathbf{v} the constant relative velocity.

2.1. *Electronic motion of the active electron; initial distributions and mono-electronic probabilities.*

2.1.1. *Model potentials*

We assume that each of the ten electrons involved in bare ion- H_2O collisions evolves independently, subject to the mean field created by the nuclei and the other nine electrons. Furthermore, we assume that the two electrons occupying the $1a_1$ molecular orbital (MO) of H_2O are too deeply bound to the O nucleus to significantly participate in the collision dynamics. We thus explicitly consider the dynamics of the eight electrons initially located in the four outermost MOs of H_2O , of symmetries $2a_1$, $1b_2$, $3a_1$ and $1b_1$.

In the CTMC calculation (see Ref. [46]), the motion of the active electron, which initially occupies the MO ϕ_k of the water molecule, is described by means of a classical distribution function, $\rho_k(\mathbf{r}, \mathbf{p}, t)$, which is discretized by using a set of N independent trajectories $\{\mathbf{r}_j(t), \mathbf{p}_j(t)\}$, according to

$$\rho_k(\mathbf{r}, \mathbf{p}, t) = \frac{1}{N} \sum_{j=1}^N \delta(\mathbf{r} - \mathbf{r}_j(t)) \delta(\mathbf{p} - \mathbf{p}_j(t)). \quad (1)$$

This discretized $\rho_k(\mathbf{r}, \mathbf{p}, t)$ is substituted in the Liouville equation $\partial \rho_k / \partial t = -\{\rho_k, h_k\}$, where $h_k(\mathbf{r}, \mathbf{p})$ is the one-electron Hamiltonian for the motion of the electron initially described by ϕ_k ; this yields the Hamilton equations:

$$\begin{aligned} \frac{\partial \mathbf{r}_j}{\partial t} &= \mathbf{p}_j \\ \frac{\partial \mathbf{p}_j}{\partial t} &= -\nabla_{\mathbf{r}_j} [h_k(\mathbf{r}_j, \mathbf{p}_j)], \end{aligned} \quad (2)$$

which monitor the temporal evolution of the j^{th} trajectory among the set of N independent ones. The one-electron Hamiltonian is expressed as:

$$h_k = \frac{p^2}{2} - \frac{Z_p}{r_p} + V_k(\mathbf{r}_t), \quad (3)$$

where \mathbf{p} is the electronic momentum and \mathbf{r}_p , \mathbf{r}_t are the electronic position vectors with respect to the projectile and the target, respectively.

In the one-center treatment, the electron in the MO ϕ_k moves in the screened Coulomb potential:

$$V_k = -\frac{Z_k}{r_O}, \quad (4)$$

where r_O is the electron distance to the oxygen nucleus and Z_k are the effective charges that fulfill:

$$Z_k = \sqrt{-2n^2\epsilon_k}, \quad (5)$$

with ϵ_k the energy of the MO ϕ_k and in the present case $n = 2$.

In the CTMC three-center treatment we have used a model potential [69] of the form:

$$V(\mathbf{r}) = V_O(r_O) + V_H(r_{H1}) + V_H(r_{H2}). \quad (6)$$

with

$$\begin{aligned} V_O(r_O) &= -\frac{8-N_O}{r_O} - \frac{N_O}{r_O} (1 + \alpha_O r_O) \exp(-2\alpha_O r_O) \\ V_H(r_H) &= -\frac{1-N_H}{r_H} - \frac{N_H}{r_H} (1 + \alpha_H r_H) \exp(-2\alpha_H r_H), \end{aligned} \quad (7)$$

which is applied to describe the motion of the electron in the four MOs of the valence shell. In these expressions r_O , r_{H1} and r_{H2} are the electron distances to the three target nuclei. To determine the parameters ($N_O = 7.1$, $N_H = (9 - N_O)/2$, $\alpha_O = 1.500 a_0$, $\alpha_H = 0.665 a_0$) we have solved the Schrödinger equation $H_0\phi_i = [p^2/2 + V(\mathbf{r})]\phi_i = \epsilon_i\phi_i$ by expanding ϕ_i in a large gaussian-type orbital (GTO) basis (see Ref. [77]). The values of the parameters are then obtained by minimizing the differences $|\epsilon_i - \epsilon_i^{\text{SCF}}|$, where ϵ_i^{SCF} are the self-consistent field (SCF) energies of the valence MOs of H₂O obtained in the same GTO basis set. In practice, we obtained $\max\{|\epsilon_i - \epsilon_i^{\text{SCF}}|, i = 1, \dots, 4\} < 10^{-3}$ a.u..

2.1.2. Initial distributions

In the one-center treatment the initial electron distribution $\rho_k(\mathbf{r}, \mathbf{p}, t = -\infty)$ can be constructed following the usual procedure for ion-H collisions. The standard method [46] employs a microcanonical distribution, $\rho_k^k(\mathbf{r}, \mathbf{p}; \epsilon_k)$, which is defined as

$$\rho_k^j(\mathbf{r}, \mathbf{p}; E_j) = \delta(h_k - E_j). \quad (8)$$

It is well-known (see e.g. Refs. [78, 79]) that the microcanonical distribution shows important limitations to describe target ionization at low collision energies; they are related to the sharp cut-off of the spatial initial distribution in the classically forbidden region (see Fig. 1). To overcome this limitation, several improved distributions have been proposed [78, 80–82]. Such improved initial conditions involve an electron energy distribution that spreads over the entire energy-bin associated to the entry channel [82] and therefore allow to mimic, to some extent, under-barrier transitions which are specially relevant for projectile charges $Z_P > 1$. In this work, we have employed a hydrogenic distribution [78] that in practice is a linear combination of 7 microcanonical distributions, ρ_k^j , with different energies E_j :

$$\rho_k(\mathbf{r}, \mathbf{p}, t \rightarrow -\infty) = \sum_{j=1}^7 a_k^j \rho_k^j(\mathbf{r}, \mathbf{p}; E_j), \quad (9)$$

where the coefficients a_k^j have been chosen by fitting the quantal position and momentum distributions, for the same one-center potential, and checked that $\sum_j a_k^j E_j \simeq \epsilon_k$. When using the hydrogenic distribution, the total ionization cross section is compatible with the Bethe limit [47], although this cross section is in general underestimated [83].

In the three-center calculations, we have limited our study to the use of microcanonical distributions, and, for simplicity, we will employ in the following a single-index notation to name them: $\rho_k(\mathbf{r}, \mathbf{p}, t = -\infty)$. To build up these distributions, we have worked by analogy with the central potential case [84], using five random parameters. In practice, the $t \rightarrow -\infty$ condition is approached by setting $Z_P = 0$ in (2) and the initial phase-space conditions are established in spherical coordinates assuming that the electron is located at the perihelion of an elliptic orbit with $\mathbf{r}_j \perp \mathbf{p}_j$ at fixed t . Thus, the five random parameters consist of (i) $\cos \theta_r$ and (ii) φ_r that define the orientation of the orbit in coordinate space; (iii) the value of β , with $0 \leq \beta \leq 1$, which yields the perihelion radius $r = \frac{r_{\max}}{2} (1 + \sqrt{1 - \beta})$, where r_{\max} is the maximum value of r that is obtained by solving numerically the nonlinear equation $V_{\text{mod}}(r_{\max}, \theta_r, \varphi_r) - \epsilon_i = 0$; (iv) the azimuthal angle φ_p of the momentum vector and (v) Δt , the time interval over which the Hamilton equations (2), with $Z_P = 0$, have to be propagated until the distribution becomes time-independent, given that the trajectories are not elliptical in the three-center V_{mod} potential.

As an illustration of the initial distributions generated by our methods, we compare in Figs. 1 and 2 the classical, $\rho_k^C(r)$, and the quantal radial distributions, $\rho_k^Q(r)$, obtained by using both one- and three-center model potentials of Eqs. (4) and (6) for the four MOs considered in this work. The classical radial distributions are defined as:

$$\rho_k^C(r) = \int d\mathbf{p} \int_0^\pi d\theta_r \sin \theta_r \int_0^{2\pi} d\varphi_r r^2 \rho_k(\mathbf{r}, \mathbf{p}), \quad (10)$$

and the quantal radial distributions have been obtained as:

$$\rho_k^Q(r) = \int_0^\pi d\theta_r \sin \theta_r \int_0^{2\pi} d\varphi_r r^2 |\phi_k(\mathbf{r})|^2. \quad (11)$$

We have checked that the plots are identical when integrating in (11) the probability densities obtained from either the SCF MOs or the MOs that are solutions or the one-electron Schrödinger equation with the model potential (6).

The shape of the microcanonical one-center radial distributions (Fig. 1) is easily understood by taking into account that the classical motion is restricted to $r < -Z_k/\epsilon_k$, which limits the extension of these distributions. To build the hydrogenic distributions we carry out a linear combination of microcanonical distributions with components of energy higher than ϵ_k , which, as already mentioned, leads to a distribution broader than the microcanonical one. The hydrogenic distributions were obtained by fitting

quantal distributions, derived from the corresponding screened Coulomb potentials. In practice, we have fitted, for each value of Z_k , the combination of the quantal radial distributions for the corresponding 2s and 2p orbitals of the form:

$$\rho_{n=2}^{\text{Q}}(r) = \frac{1}{4}\rho_{2s}^{\text{Q}}(r) + \frac{3}{4}\rho_{2p}^{\text{Q}}(r) \quad (12)$$

The comparison of the one-center distributions of Fig. 1 with both quantal and classical distributions of Fig. 2, shows that the latter are more diffuse for all MOs. This result is consistent with the fact that the potential that defines the electron motion in the MOs asymptotically behaves as $-1/r$, while $Z_k > 2$. It can be observed in Fig. 2 that the agreement between classical and quantal three-centre distributions is satisfactory over the whole r range; the classical densities are in general spread out in position space similarly to the quantal ones, although some discrepancies are noticeable for the innermost orbitals.

In Fig. 3 we compare the classical and quantal spatial densities associated to the $2a_1$, $3a_1$ and $1b_2$ MOs in the XZ plane of H_2O . $\hat{\mathbf{x}}$ corresponds to the direction between the two H atoms and $\hat{\mathbf{z}} \perp \hat{\mathbf{x}}$. In fact, the planar classical densities correspond to the fraction of electrons which initially lie within the slab $|\mathbf{y}| < 0.15 a_0$. In order to gauge the improvement inherent to the V_{mod} description of H_2O , we also report in Fig. 3 the classical densities issued from a monocentric hydrogenic classical distribution. In spite of the fact that any classical description inevitably fails to reproduce the nodal structure of the quantal densities, we see in Fig. 3 that the three-center model approach allows us to better describe the electron delocalization over the three nuclei. Moreover, the three-center classical densities concentrate on the molecular plane, while those obtained by means of the one-center treatment spread out (note the different scale employed for the plots of the one-centre distributions), as in the quantal description. We notice in Fig. 3 that the electron density of the $3a_1$ MO is well described by means of the classical V_{mod} treatment. The same happens for the $1b_1$ MO, which is not displayed in Fig. 3 because it vanishes in the molecular plane. These are positive features since the electrons should be preferentially pulled out, at low and intermediate E , from these two MOs, with the smallest ionization potentials. We shall verify this point in the next section.

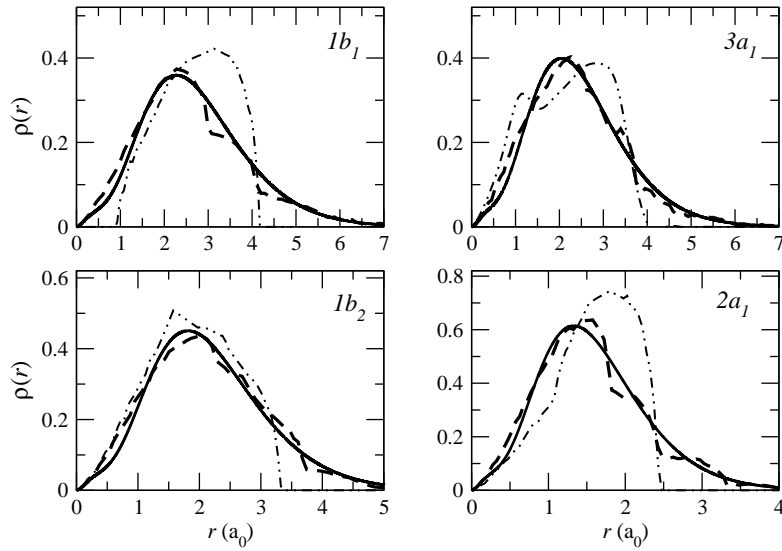


Fig. 1. Quantal (full lines), microcanonical (dotted-dashed lines) and hydrogenic distributions (dashed lines), as functions of r , for the four valence MOs of the H_2O molecule, obtained using the one-center model potential of Eq. (4) [see Eq. (12)].

2.1.3. One-electron transition probabilities

Once the initial distributions are generated, the Hamilton equations (2) are integrated up to the time $t_{\max} = 500/v$, when the one-electron ionization and capture probabilities are defined, for each of the four MOs of the valence shell ($k = 1, \dots, 4$), according to:

$$p_k^{\text{ion}} = \frac{N_k^{\text{ion}}}{N}; \quad p_k^{\text{cap}} = \frac{N_k^{\text{cap}}}{N}, \quad (13)$$

where N_k^{ion} is the number of trajectories leading to ionization (those with positive energy with respect to both projectile and target at t_{\max}) and N_k^{cap} is the number of trajectories leading to electron capture (those with negative energy with respect to the projectile at t_{\max}). The probability that the electron remains bound to the target (either in the initial or in an excited state) is therefore: $p_k^{\text{el}} = 1 - p_k^{\text{ion}} - p_k^{\text{cap}}$.

2.2. Multielectronic probabilities

In order to relate the one-electron probabilities of Eq. (13) with those of the physical many-electron system, one can apply the independent particle

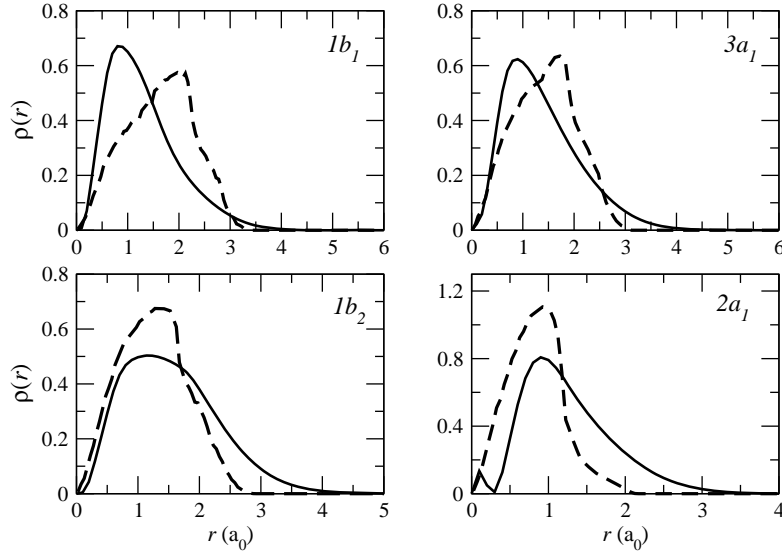


Fig. 2. Quantal (full lines) and classical (dashed lines) initial distributions $\rho(r)$ as functions of r , for the four valence MOs of the H_2O molecule, obtained using the three-center model potential of Eq. (6).

model (IPM). Assuming that the electrons occupying the same MO are equivalent, the probabilities for single ionization (SI) and single capture (SC) take the forms:

$$\begin{aligned}
 P^{\text{SI}} &= \sum_{k=1}^4 P_k^{\text{SI}} = 2 \sum_{k=1}^4 p_k^{\text{ion}} p_k^{\text{el}} \prod_{j \neq k} (p_j^{\text{el}})^2 \\
 P^{\text{SC}} &= \sum_{k=1}^4 P_k^{\text{SC}} = 2 \sum_{k=1}^4 p_k^{\text{cap}} p_k^{\text{el}} \prod_{j \neq k} (p_j^{\text{el}})^2.
 \end{aligned} \tag{14}$$

One alternative to the standard IPM is the independent event model (IEVM), suggested in Ref. [65] and used in several works (e.g. Refs. [66–68]) for ion collisions with He. Following the interpretation of Janev *et al.* [66], the IEVM assumes that the many-electron removal takes place sequentially. For ion- H_2O collisions, this means that the second electron is removed from H_2O^+ . Therefore, the implementation of the IEVM consists in substituting in (14) the elastic probabilities p_j^{el} by $\mathcal{P}_j^{\text{el}}$, where $\mathcal{P}_j^{\text{el}} = 1 - \mathcal{P}_j^{\text{ion}} - \mathcal{P}_j^{\text{cap}}$, and $\mathcal{P}_j^{\text{ion, cap}}$ are one-electron probabilities calculated for ion- H_2O^+ collisions. However, previous calculations for ion- H_2 collisions [85] indicate that the

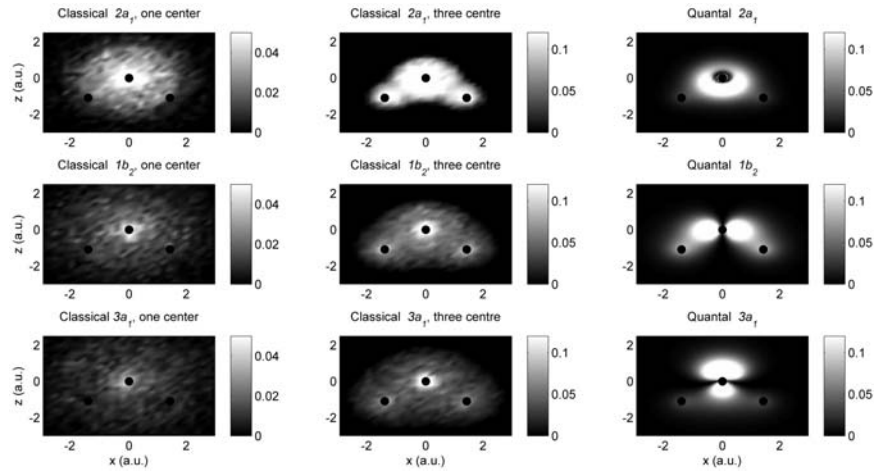


Fig. 3. Contour plots of the quantal distributions on the molecular plane ($y = 0$, right panels) and the classical distributions for those trajectories with $|y| < 0.15 a_0$ (left panels, monocentric potential; middle panels, tricentric potential) for the $2a_1$, $1b_2$ and $3a_1$ MOs. The grey scale of each panel is also shown.

electrons on the same shell are equivalent and, accordingly, we have not distinguished between ionization and capture probabilities for electrons on the same shell; this leads to:

$$\begin{aligned}
 P^{\text{SI}} &= \sum_{k=1}^4 P_k^{\text{SI}} = 2 \sum_{k=1}^4 p_k^{\text{ion}} p_k^{\text{el}} \prod_{j \neq k} (\mathcal{P}_j^{\text{el}})^2 \\
 P^{\text{SC}} &= \sum_{k=1}^4 P_k^{\text{SC}} = 2 \sum_{k=1}^4 p_k^{\text{cap}} p_k^{\text{el}} \prod_{j \neq k} (\mathcal{P}_j^{\text{el}})^2.
 \end{aligned} \tag{15}$$

These formulae can be further simplified by taking into account that $\mathcal{P}_j^{\text{ion, cap}}$ are small, because they involve electron removal from a positive ion, so that $\mathcal{P}_j^{\text{el}} \approx 1$.

We have employed this simplification in the present calculations, yielding:

$$\begin{aligned}
 P^{\text{SI}} &= 2 \sum_{k=1}^4 p_k^{\text{ion}} p_k^{\text{el}} \\
 P^{\text{SC}} &= 2 \sum_{k=1}^4 p_k^{\text{cap}} p_k^{\text{el}}
 \end{aligned} \tag{16}$$

It is well-known that processes involving the removal of more than one electron are, in general, not well described in the framework of the IPM. In this respect, we have found, taking experimental data on $H^+ + H_2O$ collisions as references, that both single and double electron processes are better described by our implementation of the IEVM (see however Refs. [68, 86]). The probabilities for transfer ionization (TI), double ionization (DI) and double capture (DC) are obtained following arguments similar to those leading to (16) as

$$P^{TI} = 2 \sum_{k=1}^4 p_k^{\text{ion}} p_k^{\text{cap}} \quad ; \quad P^{DI} = \sum_{k=1}^4 (p_k^{\text{ion}})^2 \quad ; \quad P^{DC} = \sum_{k=1}^4 (p_k^{\text{cap}})^2. \quad (17)$$

Finally, in order to compare our ionization cross sections with the available experimental data, as well as to other theoretical predictions, it is useful to define the probability of electron production (EP) (or *net* ionization), P^{EP} , as

$$P^{EP} = P^{SI} + 2P^{DI} + P^{TI} = 2 \sum_{k=1}^4 p_k^{\text{ion}}, \quad (18)$$

and, in a similar way, the *net* capture probability

$$P_{\text{net}}^C = P^{SC} + 2P^{DC} + P^{TI} = 2 \sum_{k=1}^4 p_k^{\text{cap}}, \quad (19)$$

where we have neglected the probabilities for three-electron processes.

2.3. Anisotropy and orientation averaged cross sections

The available experimental data correspond to ion collisions with gas phase targets, so that it is necessary to average the calculated cross sections over the molecule orientation to compare with them. The orientation average can be carried out in an equivalent way by averaging over the direction of the projectile velocity, keeping the molecule orientation fixed in the laboratory reference frame. Explicitly:

$$\sigma^X(v) = \frac{1}{4\pi} \int d\mathbf{b} \int d\Omega P^X(\mathbf{b}, v, \Omega), \quad (20)$$

where Ω is the solid angle that defines the direction of \mathbf{v} , and $X=SI, SC, TI, DI$ or EP . The integration has been performed numerically by applying the method of Ref. [87], where the integral over $d\Omega$ is obtained by means of a 6-point Newton-Côtes formula. The integration over $d\hat{\mathbf{b}}$ is then carried out with the restriction $\mathbf{b} \perp \mathbf{v}$, and we have considered 4 orientations

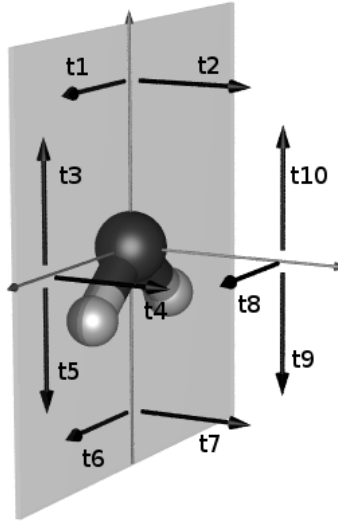


Fig. 4. Ion trajectories employed in the orientation average.

of the impact parameter \mathbf{b} in the plane perpendicular to each orientation of \mathbf{v} . Finally, taking into account the molecular symmetry, the orientation averaged cross section is given by a combination of cross sections calculated for the 10 projectile trajectories illustrated in Fig. 4:

$$\sigma^X(v) = \frac{1}{12} \left(\sum_{m=1}^{10} \sigma_m^X + \sigma_4^X + \sigma_8^X \right), \quad (21)$$

with

$$\sigma_m^X = 2\pi \int_0^\infty b P_m^X(b, v) db. \quad (22)$$

The probabilities P_m^X have been evaluated for nuclear trajectories with the orientation t_m (see Fig. 4).

In the case of employing a one-center model potential, the calculations for different trajectory orientations obviously yield the same cross section, and in order to incorporate the anisotropy effect in the total cross sections we have extended to the present case the method proposed in Ref. [47]. In this model, we assume that the minimum value of the impact parameter is equal to the dimension of the target nuclear skeleton, d , in the direction of $\hat{\mathbf{b}}$. We place the O nucleus on the origin; the H nuclei lie on the XZ half

plane with $Z < 0$ and the molecular symmetry axis is in the Z direction (Fig. 4). We consider the set of ten trajectory orientations of Fig. 4; this set includes two trajectories (t_3 and t_5) with $\hat{\mathbf{v}}$ parallel to the symmetry axis and $\hat{\mathbf{b}} = \hat{\mathbf{X}}$, where we have taken $d = 2.873/2 a_0$ (the equilibrium H-H distance in the ground state of the water molecule is $2.873 a_0$). Other two trajectories (t_6 and t_7) have $\hat{\mathbf{b}} = -\hat{\mathbf{Z}}$, where we have taken for d the distance from the O nucleus to the H-H line ($1.102 a_0$). Assuming, as in [47], that the transition probabilities are independent on the trajectory orientation, we obtain the simple expression:

$$\sigma^X(E) = 2\pi \int_0^\infty \left[b + \frac{1}{6}(1.436 + 1.102) \right] P^X(b, E) db. \quad (23)$$

3. Semiclassical calculations

We have employed two methods based on the IPM. The first one, called Method I (MI), is an expansion in terms of MOs of the supermolecule formed during the collision. The second one, Method II (MII), is an expansion in terms of many-electron configurations formed as products of the above-mentioned MOs.

3.1. Method I (MI)

In the semiclassical approach the projectile follows rectilinear trajectories with respect to the molecule, while the electron motion is treated quantum-mechanically. In the method MI, the one-electron scattering wave function, Ψ_{MI} , is solution of the eikonal equation:

$$\left(h_{\text{MI}} - i \frac{\partial}{\partial t} \right) \Psi_{\text{MI}}(\mathbf{r}, t) = 0 \quad (24)$$

with

$$h_{\text{MI}}(\mathbf{r}; \mathbf{R}) = -\frac{1}{2} \nabla^2 + V(r_t) - \frac{Z_{\text{P}}}{r_{\text{P}}}, \quad (25)$$

where we have employed a notation similar to that used in the CTMC method [see Eq. (3)]. To add additional flexibility to the description of the system, we have employed for the effective potential, $V(r_t)$, a pseudo-potential of the form:

$$V(r_{\text{O}}, r_{\text{H}_1}, r_{\text{H}_2}) = V_{\text{O}}(r_{\text{O}}) + V_{\text{H}}(r_{\text{H}_1}) + V_{\text{H}}(r_{\text{H}_2}) \quad (26)$$

with

$$V_O = -\frac{8 - N_O}{r_O} - \frac{N_O}{r_O}(1 + \alpha_O r_O)e^{-2\alpha_O r_O} |s \gg s| \\ - \frac{N_O}{r_O}(1 + \beta_O r_O)e^{-2\beta_O r_O} [1 - |s \gg s|] \quad (27)$$

$$V_H = -\frac{1 - N_H}{r_H} - \frac{N_H}{r_H}(1 + \alpha_H r_H)e^{-2\alpha_H r_H}. \quad (28)$$

As in the CTMC calculations, these expressions contain free parameters that are fitted so that the eigenvalues of the target Hamiltonian, $[h_{\text{MI}}(\mathbf{r}; \mathbf{R}) + Z_P/r_P]$ differ in less than 4×10^{-3} a.u. from the energies of the SCF MOs of water. We obtain: $N_O = 7.162$, $\alpha_O = 1.48 \text{ a}_0^{-1}$, $\beta_O = 1.60 \text{ a}_0^{-1}$ and $\alpha_H = 0.665 \text{ a}_0^{-1}$, with $N_H = (9 - N_O)/2$.

At large values R ($R_a = 1000 \text{ a}_0$ in our calculations), we solve the model-potential eigenvalue equation $h_{\text{MI}}\Phi_i = \epsilon_i\Phi_i$ in a GTO basis set $\{\xi\}$; the eigenvectors are the asymptotic molecular orbitals:

$$\Phi_i(R_a) = \sum_k c_{ik}(R_a)\xi_k(R_a) \quad (29)$$

We, then, define the frozen molecular orbitals along the projectile trajectory by using for all values of R the asymptotic matrix of MO coefficients $\mathbf{C}(R_a)$:

$$\Phi_i(R) = \sum_k c_{ik}(R_a)\xi_k(R). \quad (30)$$

It must be noted that we use the asymptotic forms of the MOs instead of an adiabatic basis of eigenfunctions of h_{MI} at each R , since in the latter case the potential energy surfaces display conical intersections, where the dynamical coupling diverge.

The one-electron wave function Ψ_{MI} is then expanded in the molecular basis set $\{\Phi\}$ as:

$$\Psi_{\text{MI}}(\mathbf{r}; t) = D(\mathbf{r}, t) \sum_j a_j(t)\Phi_j \quad (31)$$

where $D(\mathbf{r}, t)$ is a common translation factor (see [88] and references therein), which ensures that the initial conditions are fulfilled for a finite basis set. Substitution of expansion (31) into the semiclassical equation (24) leads, for each nuclear trajectory, to a system of first order differential equations:

$$i \frac{da_i}{dt} = \sum_k (\mathbf{s}^{-1}\mathbf{M})_{ik} a_k, \quad (32)$$

where

$$M_{ik} = \left\langle \Phi_i D \left| h_{\text{MI}} - i \frac{\partial}{\partial t} \right| \Phi_k D \right\rangle \quad (33)$$

and

$$s_{ik} = \langle \Phi_i D | \Phi_k D \rangle \quad (34)$$

are the coupling and overlap matrices in the basis $\{\Phi\}$. In this work, the basis set contains 108 MOs, 85 MOs, which have asymptotically positive energy, are SI channels, 7 are SEC channels, and the rest are asymptotically target MOs, including the entrance channels (the occupied orbitals of the molecule) and excitation channels. In practice, the system of differential equations (32) is solved for each of the four initial conditions: $a_j(t=0) = \delta_{ij}$, with $j = 2, 3, 4, 5$, which correspond to the electron initially located on the four valence MOs of H_2O . The one-electron probability for the transition from Φ_j to Φ_i along a given nuclear trajectory is:

$$p_{ij} = | \langle \Psi_{\text{MI}}(R_a) | \Phi_i(R_a) D \rangle |^2 = |a_i(R_a)|^2. \quad (35)$$

In practice, given the large basis employed, we have not included the translation factor and placed the origin of electronic coordinates on the oxygen nucleus, which allows us to evaluate total electron capture transition p_j^{cap} and ionization probabilities p_j^{ion} . Explicitly:

$$p_j^{\text{sec}} = \sum_i p_{ij} \quad \text{if } \epsilon_i(R_a) < 0 \quad \text{and orbital } i \text{ is on the projectile.} \quad (36)$$

$$p_j^{\text{ion}} = \sum_i p_{ij} \quad \text{if } \epsilon_i(R_a) > 0 \quad (37)$$

The many-electron probabilities are obtained from these (pseudo-potential) probabilities by using the IEVM [see Eq. (16)]:

$$P^{\text{SEC}} = 2 \sum_{j=2}^5 p_j^{\text{sec}} (1 - p_j^{\text{ion}} - p_j^{\text{sec}}) \quad ; \quad P^{\text{ION}} = 2 \sum_{j=2}^5 p_j^{\text{ion}} (1 - p_j^{\text{ion}} - p_j^{\text{sec}}) \quad (38)$$

The orientation-averaged total cross sections are then evaluated by substituting the transition probabilities (38) into Eqs. (21) and (22). Thus, for each impact velocity, the calculation involves the solution of the system of differential equations (32), with four initial conditions, for each of the ten trajectory orientations of Fig. 4. Moreover, the numerical integration of the transition probabilities of (22) requires to repeat the calculation for an appropriate set of values of b .

3.2. Method II (MII)

In this alternative multi-electronic method, we develop the scattering wavefunction in terms of configurations, which are antisymmetrized products of the asymptotic MOs Φ_i of Eq. (30). In the present calculation, the basis $\{\psi_i\}$ includes one configuration to represent the entrance channel $X^{q+} + H_2O$, with the target in the ground electronic state, where the lowest lying water orbitals Φ_i ($i = 1, \dots, 5$) are doubly occupied. The exit channels configurations are obtained as single excitations from the ground configuration:

$$\psi_1 = ||\Phi_1\bar{\Phi}_1 \dots \Phi_5\bar{\Phi}_5|| \quad \text{entrance channel} \quad (39)$$

$$\psi_j = ||\Phi_1\bar{\Phi}_1 \dots \Phi_m\bar{\Phi}_l|| + ||\Phi_1\bar{\Phi}_1 \dots \Phi_l\bar{\Phi}_m|| \quad \text{exit channels}, \quad (40)$$

where $m = 2, 3, 4$ and 5 correspond to one of the MOs of the valence shell. Φ_l , with $l \geq 6$, are the unoccupied orbitals. They can be target orbitals, and transitions to these configurations are interpreted as excitation; projectile orbitals, and the populations of these configurations are interpreted as electron capture; or, finally, when the energies of these orbitals are positive, the transitions to the corresponding configurations lead to ionization.

The collisional wave function is:

$$\Psi_{\text{MII}}(\mathbf{r}; t) = D(\mathbf{r}, t) \sum_j d_j(t) \psi_j \exp \left[-i \int_0^t dt' \Lambda_j \right] \quad (41)$$

where now \mathbf{r} denotes the coordinates of all electrons; $\Lambda_j = (\mathbf{S}^{-1} \mathbf{h}_{\text{MII}})_{jj}$, and \mathbf{S} and \mathbf{h}_{MII} are the overlap and MII Hamiltonian matrices in the basis $\{\psi\}$ (see below). This leads to the transition probabilities from state ψ_1 to state ψ_i , along trajectory k :

$$P_i^k = | \langle \Psi_{\text{MII}}(R_a) | \psi_i(R_a) D \rangle |^2 = |d_i(R_a)|^2. \quad (42)$$

The SEC probability is:

$$P^{k,\text{SEC}} = \sum_i P_i^k, \quad (43)$$

where the sum extends over the configurations representing electron capture. Analogously, SI probabilities are obtained, when the exit configurations represent ionization channels. Since the method employs the eikonal equation for all electrons, it is not necessary to use a many-electron interpretation of the one-electron transition probabilities as in the other methods employed in this work, but it requires to evaluate many two-electron

integrals. To overcome this difficulty, we have employed in the present calculation a simplification, first applied in Ref. [89], where the IPM is used to evaluate the Hamiltonian matrix in the configuration basis set. In practice:

$$\langle \psi_i | H | \psi_j \rangle \approx \langle \psi_i | h_{\text{MII}} | \psi_j \rangle = \left\langle \psi_i \left| \sum_{j=1}^{2n} h_{\text{MI}} \right| \psi_j \right\rangle \quad (44)$$

As in the other methods, the orientation-averaged cross sections are obtained integrating the transition probabilities as explained in Eqs. (21) and (22).

4. $\text{H}^+ + \text{H}_2\text{O}$ collisions.

4.1. CTMC calculations.

In this section, we compare our total cross sections to different experimental and theoretical results for the $\text{H}^+ + \text{H}_2\text{O}$ system, in the energy range $20 \text{ keV} \leq E \leq 10 \text{ MeV}$. In Fig. 5(a), we compare our cross sections for single ionization (SI) with perturbative CDW [36, 37] and FB [38] calculations and experiments [25, 27, 31]. Our calculations, using the three-center model potential and the IEVM, lead to cross sections in better agreement with the experimental ones than the one-center calculations, reported in [44], which employ a Z_{eff} description of the target and the IPM. Moreover, at high energies our SI cross section shows an energy dependence similar to that of the CDW-EIS [36, 37] and FB [38] calculations. However, it is worth pointing out the reasonable agreement of the cross section evaluated by means of the simple one-center treatment with experiments. This fact can be understood as a partial compensation of the two main differences between both one- and three-center CTMC calculations. First, the one-center model potential leads to a diffuse initial distribution (Figs. 1 and 3), which yields one-electron SI probabilities larger than those obtained in the three-center calculation. Second, the use of the conventional IPM [Eq. (14)] reduces the multielectronic SI probabilities with respect to those obtained by means of the IEVM [Eq. (16)]. This is further illustrated in Fig. 5(a), where we include the results obtained by employing the one-center model potential together with the IEVM, which clearly overestimates the SI total cross section.

We compare in Fig. 5(b) the total cross sections for electron production (EP) with the experimental data of Refs. [19] and [20] and the theoretical data of Ref. [39], issued from BGM calculations. We have also included in

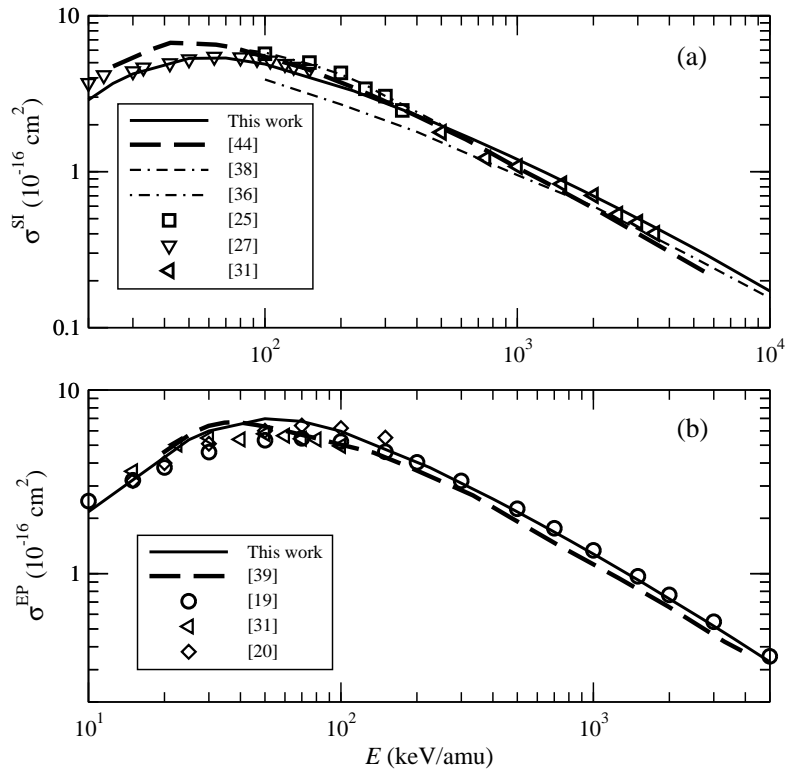


Fig. 5. Total cross sections for (a) single ionization, σ^{SI} , and (b) electron production, σ^{EP} , in proton collisions with water as functions of the collision energy. Present calculations: solid lines, CTMC with a three-center model potential and IEVM; dashed line, [44], CTMC with a one-center model potential and IPM; Other calculations: broken lines, [38], [36], [39]. Experimental results for SI: [19], [20], [25], [27], [31] (these data correspond to SI+TI for $15 < E < 100$ keV and to SI for $E > 500$ keV).

this figure the data of Ref. [31] for $E < 100$ keV/amu, which, as explained by the authors, correspond to the sum of SI and TI cross sections; indeed, double ionization is expected to be very small at low E so the EP cross section must be practically identical to the sum of SI and TI ones. Our improved CTMC results are in very good agreement with all measurements. They also nicely agree with the BGM results of Ref. [39], even though the maximum of the CTMC is located at slightly higher E than its BGM counterpart.

Our orientation-averaged SC cross section, σ^{SC} , is displayed in Fig. 6(a) as a function of the impact energy E . The figure also includes the exper-

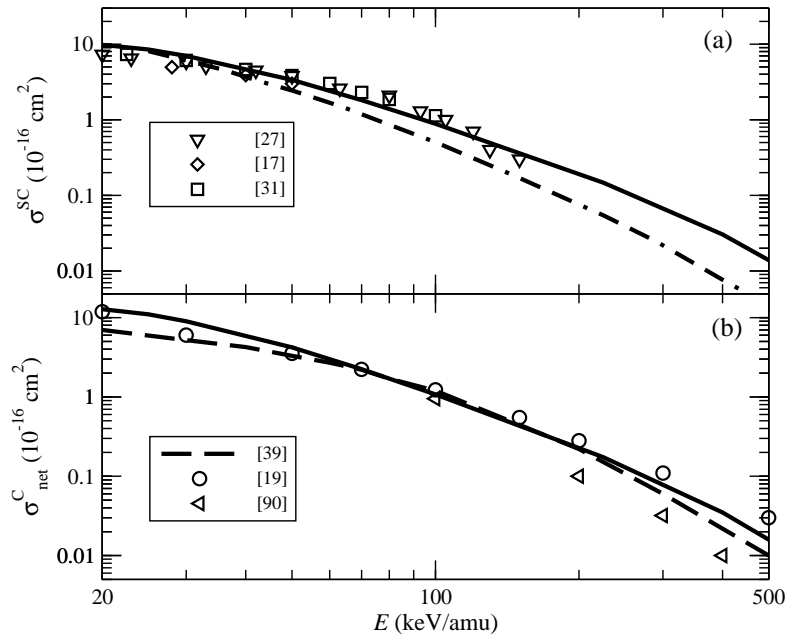


Fig. 6. Total cross sections for (a) single electron capture, σ^{SC} , and (b) net electron capture, σ_{net}^C , in proton collisions with water as functions of collision energy. Present results: solid lines, CTMC calculations using the three-center model potential and the IEVM; dotted-dashed line, CTMC calculation using the one-center model potential and the IPM. Dashed line, calculation of Ref. [39]. Experimental data for SC: [27], [17], [31], Experimental data for net electron capture: [19], [90].

imental data of Refs. [17, 27, 31]. As for the SI calculations shown in Fig. 5, the improvement inherent in the use of the three-center V_{mod} and the IEVM clearly shows up as one compares one- and three-center CTMC results, taking into account that the latter ones nicely agree with experiments over the whole impact energy range. Our computed *net* capture cross section, displayed in Fig. 6(b), is also in agreement with both the measurements [19, 90] and BGM calculations [39]. The small deviations which persist between both calculations are attributed to the liabilities of both IPM and IEVM to provide very accurate cross sections for two electron processes; here the TI contribution to *net* capture has been found to be one order of magnitude smaller than the SC one for $E > 50$ keV/amu but it can be slightly overestimated at lower E .

The dependence of the cross sections on the trajectory orientation has been discussed in detail in [45] and it will not be repeated here. A conclu-

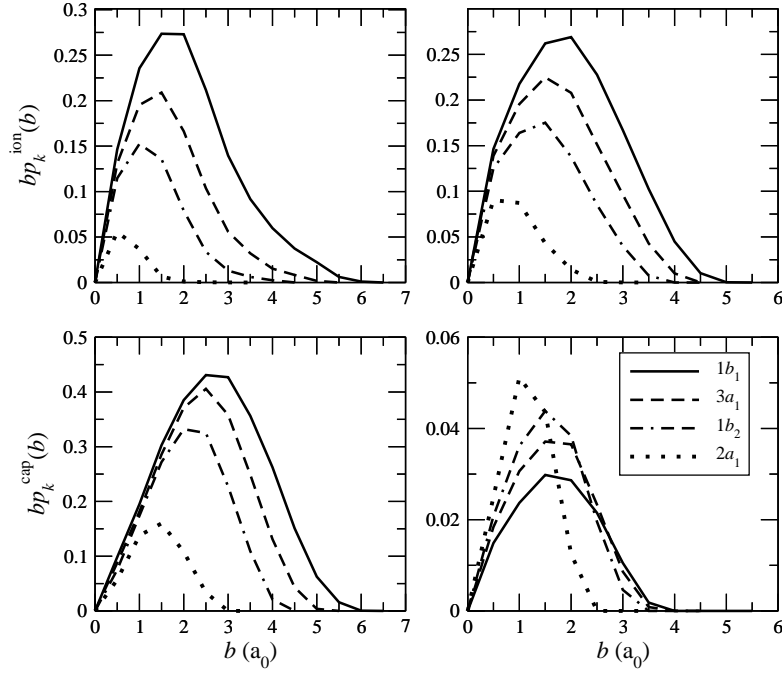


Fig. 7. One-electron transition probabilities for ionization p_k^{ion} (top panels) and capture p_k^{cap} (bottom panels), multiplied by the impact parameter, b , as functions of b for $\text{H}^+ + \text{H}_2\text{O}$ collisions at $v = 1$ a.u. (left panels) and $v = 2$ a.u. (right panels), and for the trajectory orientation described in the text.

sion of this study is that the cross section evaluated for the t_4 projectile-target orientation is such that $\sigma_4^{\text{SI}} \approx \sigma^{\text{SI}}$ for the energy range of Fig. 5 and $\sigma_4^{\text{SC}} \approx \sigma^{\text{SC}}$ at $E < 100$ keV/amu. Accordingly, we present in Fig. 7 the weighted mono-electronic ionization (bp_i^{ion}) and capture (bp_i^{cap}) probabilities, as functions of b , for each initial valence MO ϕ_i and for this representative trajectory orientation. We plot these probabilities for $v = 1$ a.u. ($E \approx 25$ keV/amu) and $v = 2$ a.u. ($E \approx 100$ keV/amu); the former impact velocity roughly corresponds to the maximum of the averaged SI cross section, where ionization and capture strongly compete with each other; $v = 2$ a.u. is representative of the high velocity regime, and we have explicitly checked that the trends found in Fig. 7 at $v = 2$ a.u. hold for higher v . We have also verified that t_m trajectories with $m \neq 4$ lead to similar features than those displayed in Fig. 7.

Concerning ionization, we observe that the more weakly bound the MO

is, the larger the corresponding p_i^{ion} ; this conforms to our intuition as well as to our experience in ion-atom collisions where it is well-known that it is generally easier to pull out an electron from a highly excited orbital. Furthermore, the weighted probabilities bp_i^{ion} peak at larger b when the initial MO is more diffuse; once again, such a behavior is intuitive and can be traced back to the spatial extension of the MO. The capture probabilities bp_i^{cap} behave as their ionization counterparts at small v ; in this velocity regime, the first steps of ionization and capture mechanisms are the same [91–93] so that it is reasonable to obtain similar trends for capture and ionization as a function of b . As v increases, we find that the contribution to the electron capture of the inner MO, $2a_1$, increases, becoming the main contribution for $v > 2.0$ a.u. ($E > 100$ keV/amu). In fact, electron capture occurs at small impact parameters, where inner shell processes are also known to be important in ion-atom systems.

4.2. *Semiclassical calculations.*

The total electron capture cross sections have been computed using methods MI and MII, and the results are compared in Fig. 8 with the CTMC results and with the experimental data. It can be noted the reasonable agreement between the results of both semiclassical calculations. In general, the MI method leads to a capture cross section in better agreement with the experiments than MII, because of the larger basis set employed in the former calculation. At $E > 20$ keV/amu, the ionization cross section is of the same order of magnitude than the capture one, and the separation of capture and ionization in the close-coupling calculation is difficult. In addition, the translation factor is not appropriate to describe ionizing transitions (see, e.g. Ref. [94]). The comparison of semiclassical and CTMC results shows a behavior similar to that found in ion-atom collisions: both methods yield similar cross sections at $E \approx 25$ keV/amu, but a smooth joining of the cross sections curves is not easy because the above-mentioned difficulty of the semiclassical calculation to disentangle capture and ionization fluxes. In addition, the classical method starts to be inappropriate at $E < 25$ keV/amu, where, in general, overestimates the capture cross section.

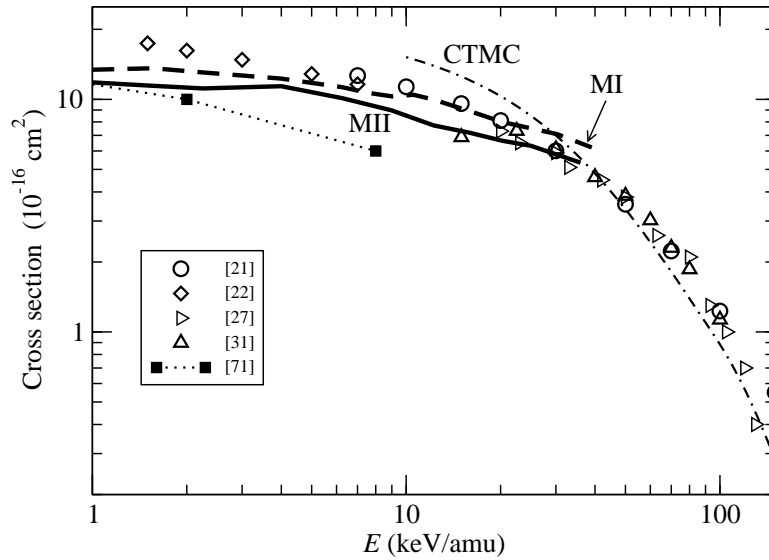


Fig. 8. SC total cross section as a function of the impact energy for $H^+ + H_2O$ collisions. Dashed line, present results using the semiclassical method MI. Full line, present results using the semiclassical method MII. Dashed-dotted line, present CTMC results. Other theoretical data: [71]. Experimental data: [21], [22], [27], [31].

5. $He^{2+} + H_2O$ collisions.

We display in Fig. 9 the cross section for electron production as a function of the impact energy E . We compare our results, obtained by means of the CTMC method with the IEVM and the three-center model potential, with the experimental data of Refs. [21, 95, 96]. Good agreement is found for $E \geq 50$ keV/amu, but discrepancies appear at lower E , where the underestimation of the experimental EP cross section can be attributed to the inaccurate computation, by means of the IEVM, of the many-electron probabilities that contribute to EP. On the other hand, the SI cross section, included in Fig. 9, largely falls down as E decreases from 50 to 10 keV/amu. Besides IEVM liabilities, the SI contribution to EP can be underestimated at low E , due to the use of microcanonical phase-space initial conditions in the CTMC calculations; such a problem is widely documented for low- E multicharged ion-atom collisions [78, 79]: in these (simple) collisional systems, it has been soon realized [78] that accurate calculations of inelastic cross sections at low and intermediate E require the use of improved initial conditions, beyond the microcanonical framework. On the other hand,

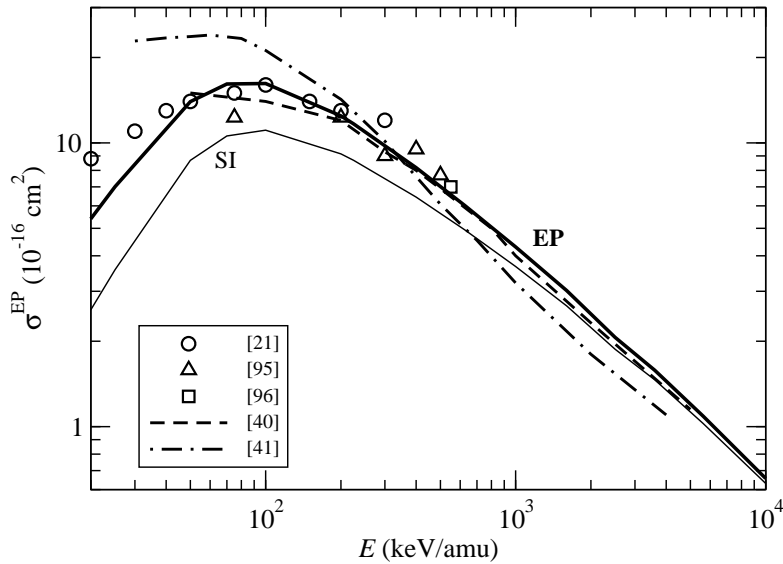


Fig. 9. Electron production cross sections as a function of the impact energy for $\text{He}^{2+} + \text{H}_2\text{O}$ collisions. Present calculations curves labeled EP and SI. Other theoretical results: [40] and [41]. Experimental results for EP: [21], [95], [96].

the over-barrier based model of Ref. [41], which do not account for target anisotropy, works worse than the present CTMC approach at any E . The FB calculations [40] behaves better at $E \geq 200$ keV/amu and coalesce, in this energy range, with the present CTMC EP cross section.

Since SC total cross sections for He^{2+} impact have not been measured at $E > 25$ keV/amu, we plot in Fig. 10 the sum of SC and TI cross sections as a function of E , and compare with the measurements of Rudd *et al.* [21] and the over-barrier calculations of Abbas *et al.* [41]. The shape of the experimental cross section is well reproduced by our calculations; nevertheless the measured and computed cross sections differ in magnitude (up to a factor of ~ 2 at low E). The TI contribution to the SC+TI cross section is found to be small over the whole impact energy range, since $\sigma_{SC} \approx \sigma_{SC} + \sigma_{TI}$ in Fig. 10. The over-barrier model [41], which yields a badly shaped cross section, does not allow to ascertain neither the experimental nor the present CTMC-IEVM values of the SC+TI cross section. New experimental investigations of both SC and TI cross sections, together with the implementation of improved calculations, would allow to elicit the validity and limitations of the IEVM at low E .

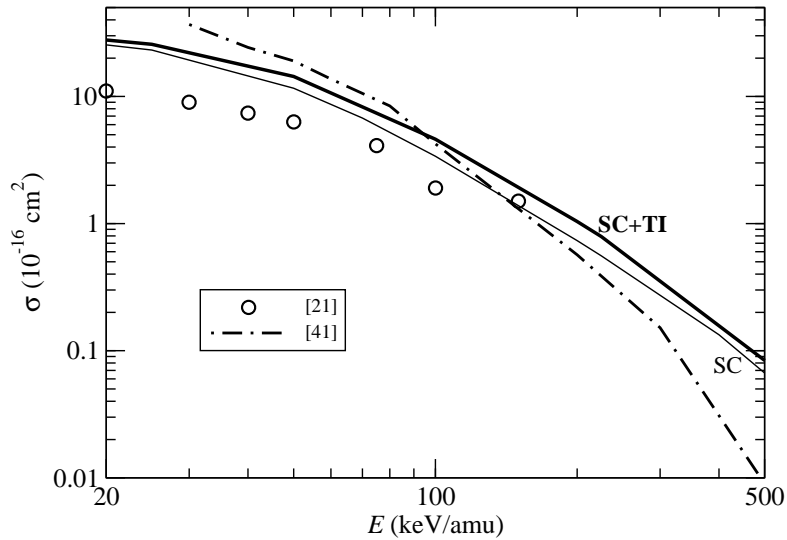


Fig. 10. Single capture plus transfer ionization (SC+TI) cross sections for $\text{He}^{2+} + \text{H}_2\text{O}$ collisions as a function of the impact energy: Solid lines, present results; dotted-dashed line, classical calculations from [41]. Experimental data: [21].

We have also evaluated the capture cross section by applying the semi-classical method MII (Fig. 11). In this result we do not find contamination by ionization at relatively high energies ($E > 10$ keV/amu), where our cross section agrees with the experimental values of Rudd *et al.* [21], with the exception of the oscillation at $E \approx 50$ keV/amu that indicates the high-energy limit of the method. At $E < 10$ keV/amu our cross section agrees with the experimental data of Refs. [22, 27], but they do not agree with the calculation of Ref. [72]. The semiclassical calculations, together with the experimental results, suggest that the CTMC method overestimates the capture cross section at $E < 60$ keV/amu.

6. $\text{C}^{6+} + \text{H}_2\text{O}$ collisions.

Drawing from the satisfactory implementations of the three-center CTMC model for H^+ and $\text{He}^{2+} + \text{H}_2\text{O}$ collisions, we have also considered C^{6+} ion impact because of its paramount importance in ion beam cancer therapy. In Fig. 12, we report our computed EP and SI cross sections as functions of E , lying in the wide range $10 \text{ keV/amu} \leq E \leq 10 \text{ MeV/amu}$. Perturbative calculations by Bernal and Liendo [42] and Dal Cappello *et al.* [43] are also

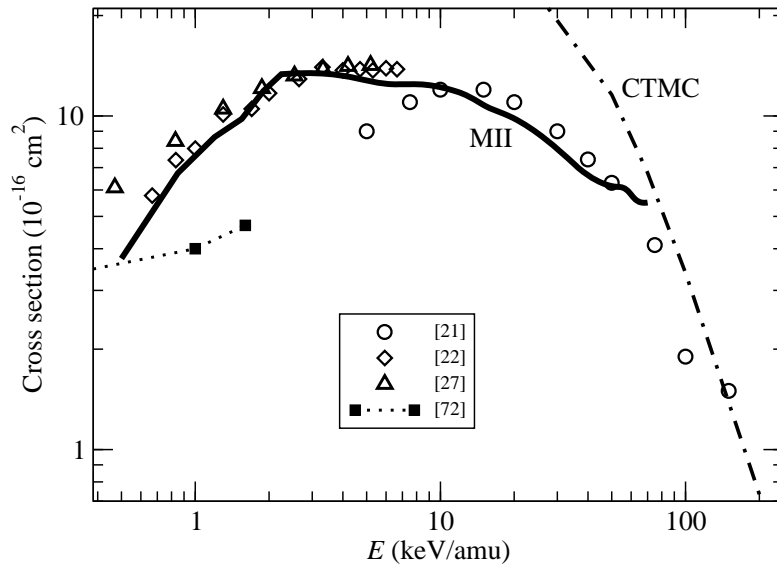


Fig. 11. SC total cross section as a function of the impact energy for $\text{He}^{2+} + \text{H}_2\text{O}$ collisions. Full line, present results using the semiclassical method MII. Dashed-dotted line, present CTMC results. Other theoretical data: [72]. Experimental data: [21], [22], [27].

included in the figure. It is clear that present CTMC and perturbative cross sections shall coalesce for $E > 10$ MeV/amu. In this respect, it has to be noted that the lower bound of validity of perturbative calculations increases with the projectile charge [83], so that particular care has to be taken before including perturbative cross sections in the Monte Carlo track structure codes that aim at describing the dynamics induced by charged particles passing through biological environments [15, 16]. We safely venture that our non-perturbative CTMC results are more accurate than those of Refs. [42, 43]; the formers lie closer to the unique experimental point at $E = 6$ MeV/amu than the latter ones. We also plot in Fig. 12 our cross sections for SC and SC+TI. As for He^{2+} collisions, we expect that the main limitation of our method is the description of two- and three-electron processes, although the estimate of σ^{TI} from Fig. 12 indicates that this process is probably not very relevant at the lowest energies of our calculations.

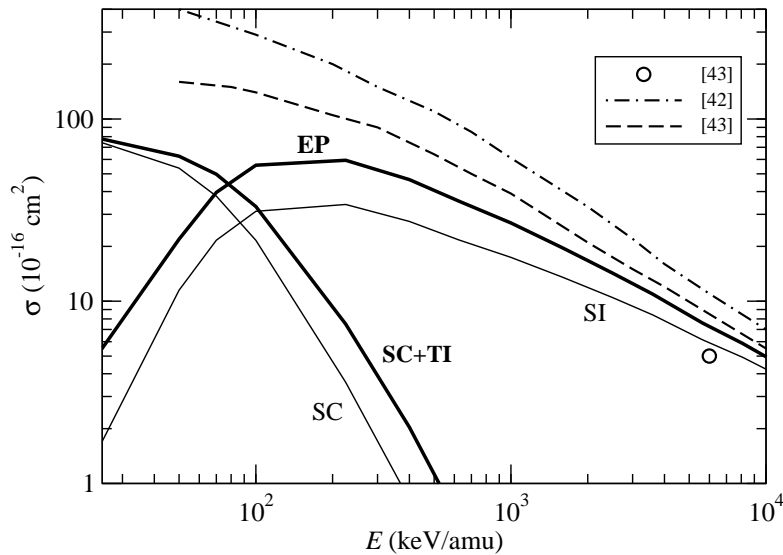


Fig. 12. Cross section as a function of the impact energy for $C^{6+}+H_2O$ collisions. Present calculations: curves labeled EP, SI, SC and SC + TI. Electron production from other calculations: [42] and [43]. Experimental point at $E = 6$ MeV/amu: [43].

7. Scaling laws and fragmentation

As stated in the Introduction, the collisional database required to model radiation damage and interaction of charged particles with biological environment is huge. In this respect, our CTMC calculations of cross sections for three ion- H_2O systems can be used to extract some scaling laws, with respect to projectile charge and impact energies, that would avoid the need for further ion- H_2O calculations. We additionally consider in this section the fragmentation processes subsequent to the primary ion- H_2O collisions. Since we have found that in general the three-center model potential approach is more accurate than the one-center model potential approximation, we limit the presentation of this section to the results of the former calculation. The results of the CTMC one-center calculation can be found in Ref. [44].

7.1. Scaling laws for ion- H_2O collisions

Most of the scaling laws that have been derived in atomic collisions stem from first-order perturbative calculations of inelastic cross sections. For

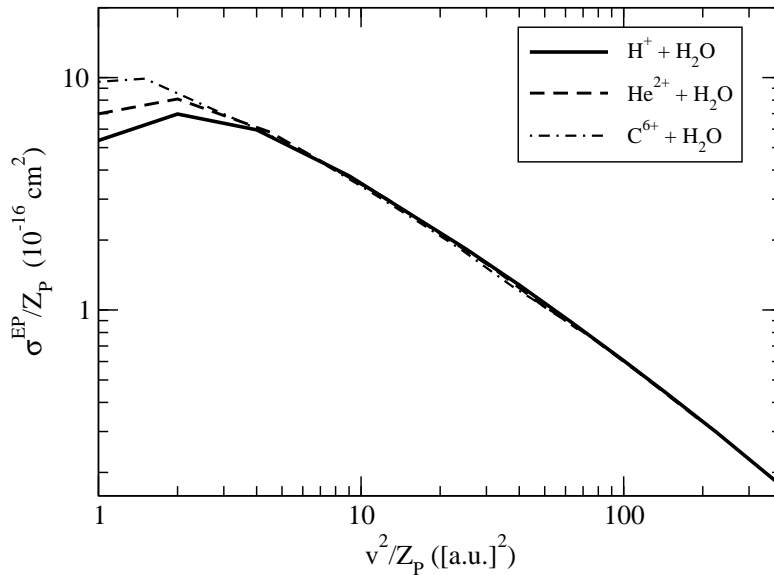


Fig. 13. Electron production cross sections over Z_P as a function of v^2/Z_P for H^+ , He^{2+} and $C^{6+}+H_2O$ collisions.

instance, FB theory indicates that ionization cross sections behave, in the high velocity regime, as $Z_P^2 \ln(E)/E$, whereas for capture, cross sections scale as Z_P^5/v^{12} [76]. These scaling relations are valid, and useful, provided the requirements for first-order perturbative conditions are fulfilled. In this respect, the perturbation strength Z_P/v is the important parameter and FB (and related laws) apply provided $Z_P/v \ll 1$.

At the energy range considered in this work, and in usual radiation damage applications, the FB validity criterion is not fulfilled for high projectile charges. As an example, the previous scaling laws are expected to fail for C^{6+} impact if $E < 1$ MeV/amu, where term orders higher than one are necessary, within perturbative expansions, to account for strong interactions between target and projectile. Introducing high-order terms in Born-type expansions is generally not a practical solution to derive simple scaling laws (non-unitarity problems can further show up), and non-perturbative calculations hide simple relations between cross sections, Z_P and v . One is thus led to derive semi-empirical relations a posteriori from calculations involving various Z_P and v for a given target. Such explicit calculations in ion-atom collisions [97, 98] have shown that ionization cross sections fall in an universal curve, in both the $Z_P/v < 1$ and $Z_P/v > 1$

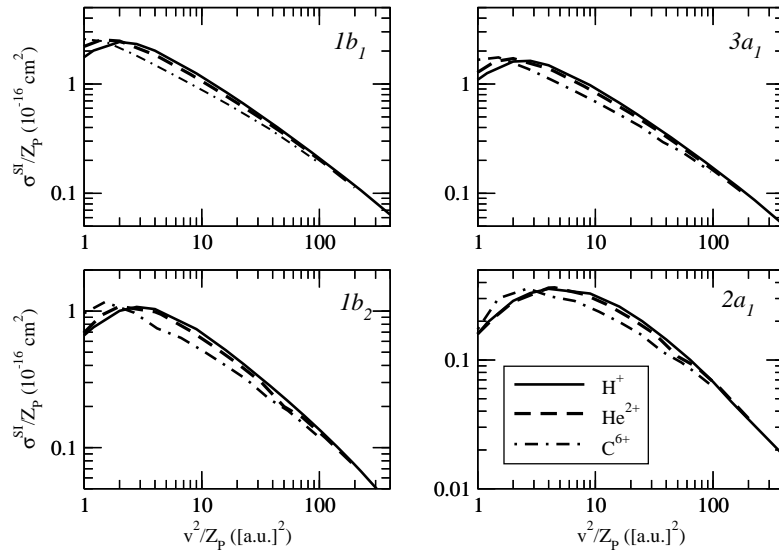


Fig. 14. Contributions to the SI cross section of the different orbitals of the valence shell of H_2O , for H^+ , He^{2+} and $\text{C}^{6+} + \text{H}_2\text{O}$ collisions. As in Fig. 13, the cross sections are divided by Z_P and plotted as functions of v^2/Z_P to check the scaling law.

regimes, if the cross section and the impact energy are linearly scaled with Z_P . In this work, we show in Fig. 13 that the same applies for EP cross sections for $E/Z_P \geq 100$ keV/amu, where $\sigma^{EP} \approx \sigma^{SI}$. The relation between σ^{EP}/Z_P and E/Z_P must not be confused with the usual Born scaling; it further allows to reproduce the strong interaction effects on the cross section when $v < Z_P$. In order to apply the scaling laws to obtain fragmentation cross sections it is useful to check that they also hold for SI cross sections from individual MOs, σ_k^{SI} ; they are obtained by using Eqs. (21)-(22) with the ionization probabilities from individual MOs: $P_k^{SI} = 2p_k^{\text{ion}} p_k^{\text{el}}$ (see Eq.(16)). This point is illustrated in Fig. 14, where we have plotted the orientation-averaged total cross sections for SI from the valence-shell MOs ($k = 2, 3, 4, 5$).

Concerning electron capture, we show in Fig. 15 that, for E ranging from ~ 100 keV/amu to ~ 1 MeV/amu, SC cross sections for multicharged ion impact can be simply, and quite accurately, scaled using H^+ reference data through $\sigma^{\text{SC}}(Z_P, v) = Z_P^2 \sigma^{\text{SC}}(1, v)$. The latter relation is in sharp disagreement with the FB capture scaling that would apply for $E \gg 1$ MeV/amu. For energies lower than 100 keV/amu, it seems that a linear scaling with respect to Z_P is better than the proposed Z_P^2 one; this agrees with the low-

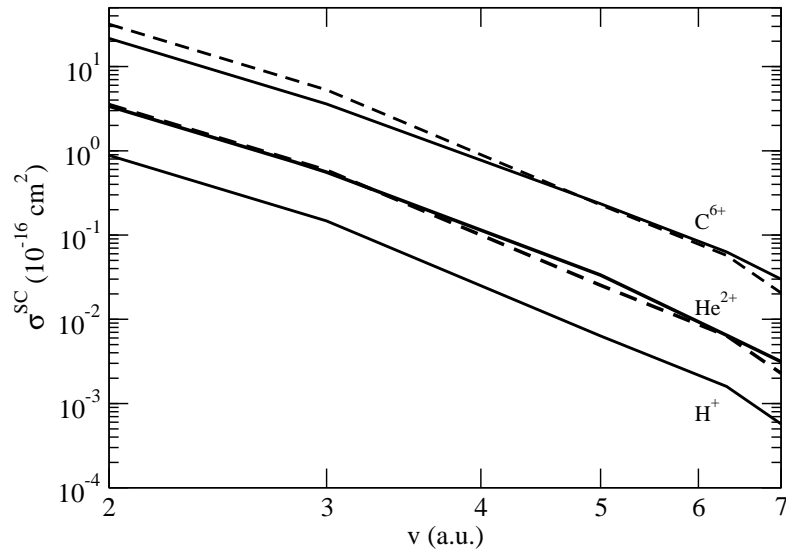


Fig. 15. Single capture cross sections as a function of the collision velocity for H^+ , He^{2+} and $C^{6+}+H_2O$ collisions. Dashed lines: proton data multiplied by Z_P^2 .

E over-barrier prediction of Knudsen *et al.* [99], which leads to constant $\sigma^{SC}(Z_P, v)/Z_P$ values for any values of Z_P and v . In other words, our proposed SC scaling fills the gap between low and high velocity regimes.

7.2. Fragmentation cross sections

Fragmentation reactions are of great importance in the radiation damage of biological systems by ion impact (see [100]) because the secondary ions formed in the fragmentation can interact with the DNA. In this work, we focus on the fragmentation processes associated to the most significant SC and SI (single) electron removals. Indeed, SC and SI can occur throughout a non-dissociative process, leading to a stable H_2O^+ fragment, and also through dissociative pathways. Under the assumption that dissociation takes place after the electron transitions [29, 31, 36], the dissociation channels consist of (i) evaporation $H_2O^+ \rightarrow OH^+ + H$, (ii) fission $H_2O^+ \rightarrow OH + H^+$ and (iii) break-up $H_2O^+ \rightarrow O^+ + H + H$. The cross sections associated to all these channels are computed by multiplying the branching ratios of Tan *et al.* [101], for fragmentation subsequent to electron removal from identified H_2O MOs, by our MO-resolved SC and SI cross sections,

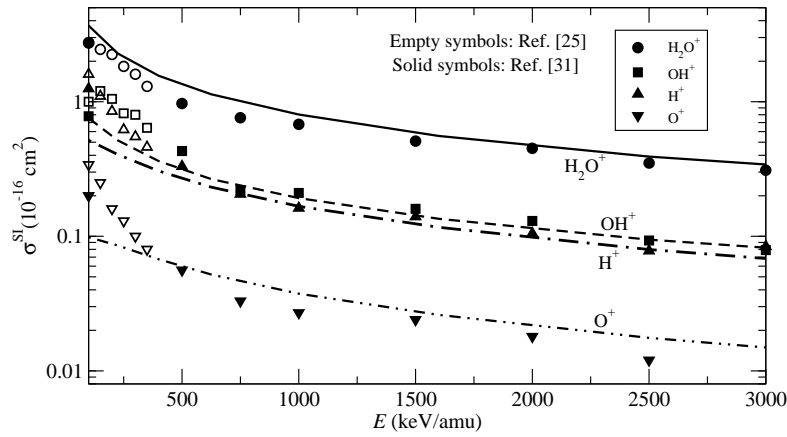


Fig. 16. Cross sections for the formation of H_2O^+ , OH^+ , H^+ and O^+ fragments (indicated in the figure) after single ionization in $\text{H}^+ + \text{H}_2\text{O}$ collisions. Lines: our calculations; Empty symbols: experimental data of Werner *et al.* [25]; solid symbols: experimental data of Luna *et al.* [31].

previously computed:

$$\begin{aligned}
 \sigma_{\text{H}_2\text{O}^+}^{\text{SC,SI}} &= 1.00 \sigma^{\text{SC,SI}}(1b_1) + 1.00 \sigma^{\text{SC,SI}}(3a_1) + 0.08 \sigma^{\text{SC,SI}}(1b_2) \\
 \sigma_{\text{OH}^+}^{\text{SC,SI}} &= 0.70 \sigma^{\text{SC,SI}}(1b_2) \\
 \sigma_{\text{H}^+}^{\text{SC,SI}} &= 0.22 \sigma^{\text{SC,SI}}(1b_2) + 0.74 \sigma^{\text{SC,SI}}(2a_1) \\
 \sigma_{\text{O}^+}^{\text{SC,SI}} &= 0.26 \sigma^{\text{SC,SI}}(2a_1).
 \end{aligned} \tag{45}$$

In practice, the fragmentation cross sections have only been computed for H^+ impact; for other projectile charges, the fragmentation cross sections can easily be derived using (45) and the scaling relations previously discussed.

In Fig. 16 we report the fragmentation cross sections after SI in the $150 \leq E \leq 3000$ keV/amu impact energy range, and compare them to the experimental results of Luna *et al.* [31] and Werner *et al.* [25]. It is worth noting that the later measurements correspond to fragmentation after either SI or TI; nonetheless, the σ^{TI} cross section is largely smaller than the σ^{SI} one in the energy range considered. It can be seen in Fig. 16 that our fragmentation cross sections are in close agreement with experiments for $E \geq 400$ keV, but significant discrepancies appear at lower E . At the relatively high collision energies of Fig. 16, the assumption of postcollisional fragmentation applies, and these discrepancies are probably a consequence of the underestimation of the ionization probability from the orbitals $1b_2$

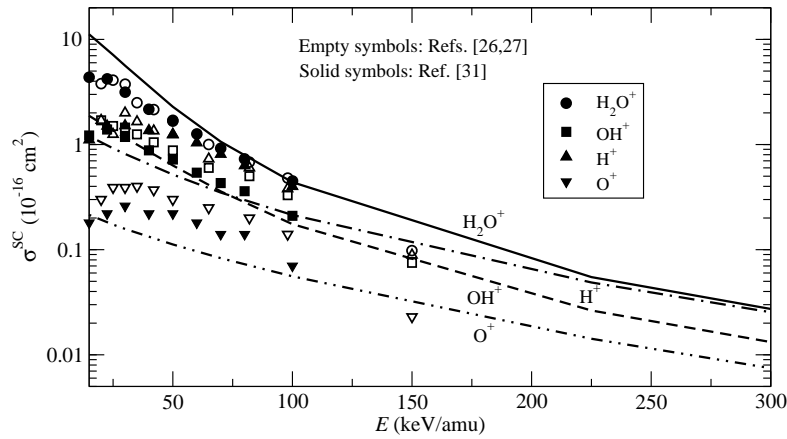


Fig. 17. Cross section for the formation of H_2O^+ , OH^+ , H^+ and O^+ fragments (indicated in the figure) after single electron capture in $\text{H}^+ + \text{H}_2\text{O}$ collisions. Lines: our calculations; Solid symbols: experimental data of Luna *et al.* [31]; empty symbols: experimental data of Gobet *et al.* [26, 27].

and $2a_1$, due to the limitations of the microcanonical initial distribution. In this respect, it has to be noted that the fragmentation cross section provides a more stringent check of accuracy of the MO-resolved SI cross sections than the total σ^{SI} to which $\sigma^{\text{SI}}(2a_1)$ little contributes (see Fig. 7).

In the energy range of Fig. 16, SI is mostly non-dissociative because it is mainly tailored by electron removal from the outer $1b_2$, $3a_1$ and $1b_1$ MOs (see Fig. 7) that favor the production of stable H_2O^+ according to (45). Furthermore, all the product cross sections present parallel shapes as functions of E for $E > 100$ keV. As explained by Montenegro *et al.* [102], this pattern shows up in the high impact velocity regime where all the MO-resolved SI cross sections exhibit the Bethe-Born $(1/I_P) \ln(E)/E$ behavior as a function of E , with I_P the ionization potential of the MO, so that according to (45), the ratios $\sigma_{\text{H}_2\text{O}^+}^{\text{SI}} : \sigma_{\text{OH}^+}^{\text{SI}} : \sigma_{\text{H}^+}^{\text{SI}} : \sigma_{\text{O}^+}^{\text{SI}}$ reduce to the constant values $[1/I_P(3a_1) + 1/I_P(1b_1) + 0.08/I_P(1b_2)] : [0.70/I_P(1b_2)] : [0.74/I_P(2a_1) + 0.22/I_P(1b_2)] : [0.26/I_P(2a_1)] = 0.1423 : 0.0368 : 0.0316 : 0.0070$.

The fragmentation cross sections (45) after single electron capture are plotted in Fig. 17 for E lying in the intermediate range 20–300 keV. Our calculations are compared to the experimental data of Luna *et al.* [31] and Gobet *et al.* [26]. As for SI, it seems that our $\sigma^{\text{SC}}(2a_1)$ cross section is underestimated for $E \leq 100$ keV so that the fission ($\sigma_{\text{H}^+}^{\text{SC}}$) and break-up ($\sigma_{\text{O}^+}^{\text{SC}}$)

cross sections lie below the measurements, while $\sigma_{\text{H}_2\text{O}^+}^{\text{SC}}$ and $\sigma_{\text{OH}^+}^{\text{SC}}$ are in satisfactory agreement with the data of Luna *et al.*. The most conspicuous difference between fragmentation cross sections after SC from those after SI (Figs. 17 and 16, respectively) is the fact that in the former case the lines are not parallel. However, one can note in this figure that the lines for non-dissociative and evaporation reactions, and also those for fission and break up processes, are parallel. To explain this fact, one has to take into account that cross sections for fission and break up reactions are dominated by the contribution of the $2a_1$ MO, and, as explained in section III, the SC probability from this MO increases with E , becoming clearly dominant at high E , while a similar effect is not observed in SI. Hence, the energy dependence of $\sigma^{\text{SC}}(2a_1)$ changes the slope of fission and break up lines and does not affect to the other two lines of Fig. 17. This effect also explains that $\sigma_{\text{H}^+}^{\text{SC}}$ attains similar values to that of $\sigma_{\text{H}_2\text{O}^+}^{\text{SC}}$ at high energies.

8. Conclusions

We have employed an improved impact parameter-CTMC model to calculate cross sections for single ionization, single capture, and two-electron processes (transfer ionization, double capture and double ionization) in H^+ , He^{2+} , $\text{C}^{6+}+\text{H}_2\text{O}$ collisions in an impact energy range $20 \leq E \leq 10000$ keV/amu that largely encompasses the intermediate and high energy regimes of interest for ion-based cancer therapy applications. In the framework of the independent electron approximation, our improved model employs a three-center model potential to describe the interaction of the active electron with the H_2O^+ core, beyond the usual one-center Z_{eff} description. This has allowed us to explicitly consider anisotropy effects related to the multi-center nature of the target. The evaluation of inelastic probabilities for the physical many-electron system has been performed by means of the independent event model (IEVM) which has been found to be more accurate than the usual independent particle model (IPM). Moreover, the new results with a three-center model potential lie close to the basis generator method (BGM) results of Lüdde *et al.* [see Figs. 5(b) and 6(b)]. In order to extend the calculation to lower energies, we have carried out semiclassical calculations of SEC total cross sections employing molecular bases and using simplified methods based on the IPM and IEVM approximations. The calculated cross sections show reasonable agreement with the experiments, and the overlap between classical and semiclassical results is similar to that found for ion-atom collisions.

For $\text{He}^{2+} + \text{H}_2\text{O}$, the three-center CTMC description provided cross sections in better agreement with the experimental data than the over-barrier model of Abbas *et al.* [41] (see Figs.9 and 10). C^{6+} impact has also been considered because of its great importance in ion beam cancer therapy, in a wide impact energy range beyond the scope of perturbative approaches (see Fig. 12).

The explicit calculations of cross sections for the three above-mentioned systems have allowed us to extract some scaling laws, with respect to projectile charge Z_P and impact energies E , for electron production and single capture cross sections (see Figs. 13 and 15). Such scaling laws are useful to fill in the gaps (in Z_P and E) which exist in the collisional database. In addition, the scaling relations that apply to bare projectile impact can be safely used for dressed projectiles at intermediate E when inner electronic structure is not important [47, 76]. Finally, as a stringent test of the calculations, we have computed the fragmentation cross sections associated to the single ionization and single capture processes (see Figs. 16 and 17) using the three-center CTMC method. The non-dissociative and evaporation ($\text{H}_2\text{O}^+ \rightarrow \text{OH}^+ + \text{H}$) cross sections present satisfactory agreement with measurements from low to high impact energies whereas the fission ($\text{H}_2\text{O}^+ \rightarrow \text{OH} + \text{H}^+$) and break-up ($\text{H}_2\text{O}^+ \rightarrow \text{O}^+ + \text{H} + \text{H}$) ones are underestimated at low E because of a primary underestimation of the cross sections for electron removal from the innermost $2a_1$ MO, which is practically unnoticeable in the total cross sections.

In this work we have shown that the use of effective potentials allows us to extend the application of methods, widely employed in ion-atom collisions, to the treatment of ion collisions with complex molecules. Future work along this line will involve a detailed study of the independent electron approximation in both CTMC and semiclassical treatments, including numerical calculations of ion collisions with other molecular systems. The main goal of future work is to implement a methodology for evaluating cross sections for other ion-biomolecule collisions, relevant in radiation damage of biological systems.

Acknowledgments

This work has been partially supported by CCG08-UAM/ESP3990 project and the DGICYT project ENE2007-62934. The use of the computational facilities at the CCC of the Universidad Autónoma de Madrid is gratefully acknowledged.

References

- [1] U. Amaldi and G. Kraft, *Rep. Prog. Phys.* **68**, 1861–1882 (2005).
- [2] D. Schardt, T. Elsässer, and D. Schulz-Ertner, *Rev. Mod. Phys.* **82**, 383–425 (2010).
- [3] J. R. Castro, D. E. Linstadt, J.-P. Bahary, P. L. Petti, I. Daftari, J. Collier, P. H. Gutin, G. Gauger, and T. L. Phillips, *Int. J. Radiat. Oncol. Biol. Phys.* **29**, 647 – 655 (1994).
- [4] H. Tsujii, S. Morita, T. Miyamoto, J. Mizoe, H. Katou, H. Tsuji, S. Yamada, N. Yamamoto, and H. Murata, *Progress in radio-oncology VII, Monduzzi Editore, Bologna, Italy*. p. 393 (2002).
- [5] D. Schulz-Ertner, A. Nikoghosyan, C. Thilman, T. Haberer, O. Jkel, C. Karger, G. Kraft, M. Wannenmacher, and J. Debus, *Int. J. Radiat. Oncol. Biol. Phys.* **58**, 631 – 640 (2004).
- [6] M. Krämer, O. Jäkel, T. Haberer, G. Kraft, D. Schardt, and U. Weber, *Physics in Medicine and Biology*. **45**, 3299 – 3317 (2000).
- [7] M. Krämer and M. Scholz, *Phys. Med. Biol.* **45**, 3319 – 3330 (2000).
- [8] O. Jäkel, G. Hartmann, C. Karger, P. Heeg, and J. Rassow, *Med. Phys.* **27**, 1588–1600 (2000).
- [9] M. Scholz, A. Kellerer, W. Kraft-Weyrather, and G. Kraft, *Radiat. Environ Biophys.* **36**, 59–66 (1997).
- [10] F. Ballarini, D. Alloni, A. Facoetti, and A. Ottolenghi, *New Journal of Physics*. **10**, 075008–1 – 075008–17 (2008).
- [11] J. de Vries, R. Hoekstra, R. Morgenstern, and T. Schlathölter, *Phys. Rev. Lett.* **91**, 053401–1–053401–4 (2003).
- [12] M. C. Bacchus-Montabonel, M. Labuda, Y. S. Tergiman, and J. E. Sienkiewicz, *Phys. Rev. A*. **72**, 052706–1–052706–9 (2005).
- [13] M. C. Bacchus-Montabonel, Y. S. Tergiman, and D. Talbi, *Phys. Rev. A*. **79**, 012710–1– 012710–7 (2009).
- [14] B. Boudaïffa, P. Cloutier, D. Hunting, M. A. Huels, and L. Sanche, *Science*. **287**, 1658–1660 (2000).
- [15] S. Uehara, L. Toburen, and H. Nikjoo, *Int. J. Radiat. Biol.* **77**, 139–154 (2001).
- [16] S. Uehara and H. Nikjoo, *J. Phys. Chem. B*. **106**, 11051–11063 (2002).
- [17] R. Dagnac, D. Blanc, and D. Molina, *J. Phys. B: At. Mol. Opt. Phys.* **3** (9), 1239–1251 (1970).
- [18] M. E. Rudd, R. D. Dubois, L. H. Toburen, C. A. Ratcliffe, and T. V. Goffe, *Phys. Rev. A*. **28**, 3244–3257 (1983).
- [19] M. E. Rudd, T. V. Goffe, R. D. DuBois, and L. H. Toburen, *Phys. Rev. A*. **31**, 492–494 (1985).
- [20] M. A. Bolorizadeh and M. E. Rudd, *Phys. Rev. A*. **33**, 888–892 (1986).
- [21] M. E. Rudd, T. V. Goffe, and A. Itoh, *Phys. Rev. A*. **32**, 2128–2133 (1985).
- [22] J. B. Greenwood, A. Chutjian, and S. J. Smith, *Astrophys. J.* **529**, 605–609 (2000).
- [23] R. J. Mawhorter, A. Chutjian, T. E. Cravens, N. Djurić, S. Hossain, C. M. Lisse, J. A. MacAskill, S. J. Smith, J. Simcic, and I. D. Williams, *Phys.*

- Rev. A.* **75**, 032704–1–032704–7 (2007).
- [24] B. Seredyuk, R. W. McCullough, H. Tawara, H. B. Gilbody, D. Bodewits, R. Hoekstra, A. G. G. M. Tielens, P. Sobocinski, D. PešićPestic, R. Hellhammer, B. Sulik, N. Stolterfoht, O. Abu-Haija, and E. Y. Kamber, *Phys. Rev. A.* **71**, 022705–1–022705–7 (2005).
- [25] U. Werner, K. Beckord, J. Becker, and H. O. Lutz, *Phys. Rev. Lett.* **74**, 1962–1965 (1995).
- [26] F. Gobet, B. Farizon, M. Farizon, M. J. Gaillard, M. Carré, M. Lezius, P. Scheier, and T. D. Märk, *Phys. Rev. Lett.* **86**, 3751–3754 (2001).
- [27] F. Gobet, S. Eden, B. Coupier, J. Tabet, B. Farizon, M. Farizon, M. J. Gaillard, M. Carré, S. Ouaskit, T. D. Märk, and P. Scheier, *Phys. Rev. A.* **70**, 062716–1–062716–8 (2004).
- [28] F. Alvarado, R. Hoekstra, and T. Schlathölter, *J. Phys. B: At. Mol. Opt. Phys.* **38**, 4085–4094 (2005).
- [29] H. Luna and E. C. Montenegro, *Phys. Rev. Lett.* **94**, 043201–1–043201–4 (2005).
- [30] P. Sobocinski, Z. D. Pešić, R. Hellhammer, N. Stolterfoht, B. Sulik, S. Legendre, and J.-Y. Chesnel, *J. Phys. B: At. Mol. Opt. Phys.* **38**, 2495–2504 (2005).
- [31] H. Luna, A. L. F. de Barros, J. A. Wyer, S. W. J. Scully, J. Lecointre, P. M. Y. Garcia, G. M. Sigaud, A. C. F. Santos, V. Senthil, M. B. Shah, C. J. Latimer, and E. C. Montenegro, *Phys. Rev. A.* **75**, 042711–1–042711–11 (2007).
- [32] M. N. Monce, S. Pan, N. L. Radeva, and J. L. Pepper, *Phys. Rev. A.* **79**, 012704–1–012704–4 (2009).
- [33] B. D. Goldman, S. A. Timpone, M. N. Monce, L. Mitchell, and B. Griffin, *Phys. Rev. A.* **83**(4), 042701–1–042701–7 (2011).
- [34] D. Belkić, *J. Math. Chem.* **47**, 1366–1419 (2010).
- [35] P. D. Fainstein, G. H. Olivera, and R. D. Rivarola, *Nucl. Instr. and Meth. B.* **107**, 19–26 (1996).
- [36] G. H. Olivera, C. Caraby, P. Jardin, A. Cassimi, L. Adoui, and B. Gervais, *Physics in Medicine and Biology.* **43**, 2347–2360 (1998).
- [37] B. Gervais, M. Beuve, G. H. Olivera, and M. E. Galassi, *Radiat. Phys. Chem.* **75**, 493–513 (2006).
- [38] O. Boudrioua, C. Champion, C. D. Cappello, and Y. V. Popov, *Phys. Rev. A.* **75**, 022720–1–022720–9 (2007).
- [39] H. J. Lüdde, T. Spranger, M. Horbatsch, and T. Kirchner, *Phys. Rev. A.* **80**, 060702–1–060702–4 (2009).
- [40] C. Champion, O. Boudrioua, C. Dal Cappello, Y. Sato, and D. Ohsawa, *Phys. Rev. A.* **75**, 032724–1–032724–9 (2007).
- [41] I. Abbas, C. Champion, B. Zarour, B. Lasri, and J. Hassen, *Physics in Medicine and Biology.* **53**, N41–N51 (2008).
- [42] M. A. Bernal and J. A. Liendo, *Nucl. Instr. and Meth. B.* **262**, 1–6 (2007).
- [43] C. D. Cappello, C. Champion, O. Boudrioua, H. Lekadir, Y. Sato, and D. Ohsawa, *Nucl. Instr. and Meth. B.* **267**, 781–790 (2009).
- [44] L. F. Errea, C. Illescas, L. Méndez, B. Pons, I. Rabadán, and A. Riera,

- Phys. Rev. A.* **76**, 040701–1–040701–4 (2007).
- [45] C. Illescas, L. F. Errea, L. Méndez, B. Pons, I. Rabadán, and A. Riera, *Phys. Rev. A.* **83**, 052704–1–052704–12 (2011).
- [46] R. Abrines and I. C. Percival, *Proc. Phys. Soc.* **88**, 861–872 (1966).
- [47] C. Illescas and A. Riera, *Phys. Rev. A.* **60**, 4546–4560 (1999).
- [48] L. F. Errea, C. Illescas, L. Méndez, B. Pons, A. Riera, and J. Suárez, *J. Phys. B: At. Mol. Opt. Phys.* **37**, 4323–4338 (2004).
- [49] L. F. Errea, C. Illescas, L. Méndez, B. Pons, A. Riera, and J. Suárez, *J. Phys. B: At. Mol. Opt. Phys.* **39**, L91–L97 (2006).
- [50] L. F. Errea, F. Guzmán, C. Illescas, L. Méndez, B. Pons, A. Riera, and J. Suárez, *Plasma Physics and Controlled Fusion*. **48**, 1585–1604 (2006).
- [51] F. Guzmán, L. F. Errea, C. Illescas, L. Méndez, and B. Pons, *J. Phys. B: At. Mol. Opt. Phys.* **43**, 144007–1–144007–8 (2010).
- [52] C. L. Kirschbaum and L. Wilets, *Phys. Rev. A.* **21**, 834–841 (1980).
- [53] J. S. Cohen, *Phys. Rev. A.* **54**, 573–586 (1996).
- [54] F. Guzmán, L. F. Errea, and B. Pons, *Phys. Rev. A.* **80**, 042708–1–042708–9 (2009).
- [55] J. H. McGuire and L. Weaver, *Phys. Rev. A.* **16**, 41–47 (1977).
- [56] V. A. Sidorovich, *J. Phys. B: At. Mol. Phys.* **14**, 4805–4823 (1981).
- [57] H. J. Lüdde and R. M. Dreizler, *J. Phys. B: At. Mol. Opt. Phys.* **18**, 107–112 (1985).
- [58] C. O. Reinhold and C. A. Falcón, *J. Phys. B: At. Mol. Opt. Phys.* **21**, 1829–1843 (1988).
- [59] L. Meng, C. O. Reinhold, and R. E. Olson, *Phys. Rev. A.* **40**, 3637–3645 (1989).
- [60] L. Meng, C. O. Reinhold, and R. E. Olson, *Phys. Rev. A.* **42**, 5286–5291 (1990).
- [61] C. Illescas and A. Riera, *J. Phys. B: At. Mol. Opt. Phys.* **31**, 2777–2793 (1998).
- [62] S. Otranto, R. E. Olson, and P. Beiersdorfer, *J. Phys. B: At. Mol. Opt. Phys.* **40**, 1755–1766 (2007).
- [63] S. Otranto and R. E. Olson, *Phys. Rev. A.* **77**, 022709–1–022709–9 (2008).
- [64] C. Champion and R. D. Rivaola, *Phys. Rev. A.* **82**, 042704–1–042704–8 (2010).
- [65] D. S. F. Crothers and R. McCarroll, *J. Phys. B: At. Mol. Phys.* **20**, 2835–2842 (1987).
- [66] R. K. Janev, E. A. Solov'ev, and D. Jakimovski, *J. Phys. B: At. Mol. Opt. Phys.* **28**, L615–L620 (1995).
- [67] L. A. Wehrman, A. L. Ford, and J. F. Reading, *J. Phys. B: At. Mol. Opt. Phys.* **29**, 5831–5842 (1996).
- [68] J. Bradley, R. J. S. Lee, M. McCartney, and D. S. F. Crothers, *J. Phys. B: At. Mol. Opt. Phys.* **37**, 3723–3734 (2004).
- [69] L. Méndez, L. F. Errea, C. Illescas, I. Rabadán, B. Pons, and A. Riera, *AIP Conf. Proc.* **1080**, 51–58 (2008).
- [70] H. Getahun, L. F. Errea, C. Illescas, L. Méndez, and I. Rabadán, *Eur. Phys. J. D.* **60**, 45–49 (2010).

- [71] S. Mada, K. N. Hida, M. Kimura, L. Pichl, H.-P. Liebermann, Y. Li, and R. J. Buenker, *Phys. Rev. A* **75**, 022706–1–022706–7 (2007).
- [72] R. Cabrera-Trujillo, E. Deumens, Y. Ohrn, O. Quinet, J. R. Sabin, and N. Stolterfoht, *Phys. Rev. A* **75**, 052702–1–052702–13 (2007).
- [73] O. L. Polyansky, A. G. Császár, S. V. Shirin, N. F. Zobov, P. Barletta, J. Tennyson, D. W. Schwenke, and P. J. Knowles, *Science* **299**, 539–542 (2003).
- [74] T. Rajamäki, A. Miani, and L. Halonen, *J. Chem. Phys.* **118**, 10929–10938 (2003).
- [75] L. F. Errea, A. Macías, L. Méndez, I. Rabadán, A. Riera, A. Rojas, and P. Sanz, *Phys. Rev. A* **63**, 062713–1–062713–9 (2001).
- [76] B. H. Bransden and M. H. C. McDowell, *Charge Exchange and the Theory of Ion-Atom Collisions*. Oxford, Clarendon (1992).
- [77] I. Rabadán, L. F. Errea, P. Martínez, and L. Méndez, *AIP Conf. Proc.* **1080**, 98–103 (2008).
- [78] D. J. W. Hardie and R. E. Olson, *J. Phys. B: At. Mol. Phys.* **16**, 1983–1996 (1983).
- [79] G. Peach, S. L. Willis, and M. R. C. McDowell, *J. Phys. B: At. Mol. Phys.* **18**, 3921–3937 (1985).
- [80] J. S. Cohen, *J. Phys. B: At. Mol. Opt. Phys.* **18**, 1759–1769 (1985).
- [81] M. J. Raković, D. R. Schultz, P. C. Stancil, and R. K. Janev, *J. Phys. A: Math. Gen.* **34**, 4753–4770 (2001).
- [82] L. F. Errea, C. Illescas, L. Méndez, B. Pons, A. Riera, and J. Suárez, *Phys. Rev. A* **70**, 52713–1–52713–12 (2004).
- [83] L. F. Errea, L. Méndez, B. Pons, A. Riera, I. Sevilla, and J. Suárez, *Phys. Rev. A* **74**, 012722–1–012722–17 (2006).
- [84] C. Illescas, I. Rabadán, and A. Riera, *J. Phys. B: At. Mol. Opt. Phys.* **30**, 1765–1784 (1997).
- [85] D. Elizaga, L. F. Errea, J. D. Gorfinkiel, C. Illescas, L. Méndez, A. Macías, A. Riera, A. Rojas, O. J. Kroneisen, T. Kirchner, H. J. Lüdde, A. Henne, and R. M. Dreizler, *J. Phys. B: At. Mol. Opt. Phys.* **32**, 857–875 (1999).
- [86] A. L. Ford, L. Wehrman, K. A. Hall, and J. F. Reading, *J. Phys. B: At. Mol. Opt. Phys.* **30**, 2889–2897 (1997).
- [87] L. F. Errea, J. D. Gorfinkiel, A. Macías, L. Méndez, and A. Riera, *J. Phys. B: At. Mol. Opt. Phys.* **30**, 3855–3872 (1997).
- [88] L. F. Errea, C. Harel, H. Jouin, L. Méndez, B. Pons, and A. Riera, *J. Phys. B: At. Mol. Opt. Phys.* **27**, 3603–3634 (1994).
- [89] L. Errea, J. D. Gorfinkiel, C. Harel, H. Jouin, A. Macías, L. Méndez, B. Pons, and A. Riera, *J. Phys. B: At. Mol. Opt. Phys.* **33**, 3107–3122 (2000).
- [90] L. H. Toburen, M. Y. Nakai, and R. A. Langley, *Phys. Rev.* **171**, 114–122 (1968).
- [91] C. Illescas, I. Rabadán, and A. Riera, *Phys. Rev. A* **57**, 1809–1820 (1998).
- [92] L. F. Errea, C. Harel, C. Illescas, H. Jouin, L. Méndez, B. Pons, and A. Riera, *J. Phys. B: At. Mol. Opt. Phys.* **31**, 3199–3214 (1998).
- [93] E. A. Solov'ev, *J. Phys. B: At. Mol. Opt. Phys.* **38**, R153–R194 (2005).

- [94] L. F. Errea, C. Harel, H. Jouin, L. Méndez, B. Pons, A. Riera, and I. Sevilla, *Phys. Rev. A* **65**, 022711–1–022711–9 (2002).
- [95] L. H. Toburen, W. E. Wilson, and R. J. Popowich, *Radiation Research*. **82**, 27–44 (1980).
- [96] P. S. Rudolph and C. E. Melton, *J. Chem. Phys.* **45**, 2227–2235 (1966).
- [97] A. S. Schlachter, K. H. Berkner, W. G. Graham, R. V. Pyle, P. J. Schneider, K. R. Stalder, J. W. Stearns, J. A. Tanis, and R. E. Olson, *Phys. Rev. A* **23**, 2331–2339 (1981).
- [98] H. Knudsen, L. H. Andersen, P. Hvelplund, G. Astner, H. Cederquist, H. Danared, L. Liljeby, and K. G. Rensfelt, *J. Phys. B: At. Mol. Opt. Phys.* **17**, 3545–3564 (1984).
- [99] H. Knudsen, H. K. Haugen, and P. Hvelplund, *Phys. Rev. A* **23**, 597–610 (1981).
- [100] N. J. Mason, *AIP Conf. Proc.* **1080**, 3–20 (2008).
- [101] K. H. Tan, C. E. Brion, P. E. Van der Leeuw, and M. J. Van der Wiel, *Chem. Phys.* **29**, 299–309 (1978).
- [102] E. C. Montenegro, S. W. J. Scully, J. A. Wyer, V. Senthil, and M. B. Shah, *J. Electron. Spectros. Relat. Phenom.* **155**, 81–85 (2007).